Antidiabetic and antioxidant potential of Oenocarpus bataua Mart: a metabolomic and in silico study

Noroska G. S. Mogollón
Universidad Regional Amazónica IKIAM
Karel Diéguez-Santana
Universidad Regional Amazónica IKIAM
Carlos A. Méndez-Durazno
Pontificia Universidad Católica del Ecuador
Thomas Garzón
Universidad Regional Amazónica IKIAM
Jefferson Pastuña-Fasso
Universidad Regional Amazónica IKIAM
Roberth Reyes
Universidad Regional Amazónica IKIAM
Katterine Olalla-Tacuri
Universidad Regional Amazónica IKIAM
José R. Almeida
Universidad Regional Amazónica IKIAM
Melanie Ochoa-Ocampo
Universidad Regional Amazónica IKIAM
Pablo Cisneros-Pérez
Universidad Yachay Tech
Patricio Espinoza-Montero
pespinoza646@puce.edu.ec

Pontificia Universidad Católica del Ecuador

Article

Keywords: antidiabetic, secondary metabolites, antioxidant activity, molecular docking, ADMET

Posted Date: March 25th, 2026

DOI: https://doi.org/10.21203/rs.3.rs-8971643/v1

Additional Declarations: No competing interests reported.

Antidiabetic and antioxidant potential of Oenocarpus bataua Mart: a metabolomic and in silico study

Noroska G. S. Mogollón[1,+], Karel Diéguez-Santana[1,+], Carlos Alberto Méndez-Durazno[2], Thomas Garzón[1], Jefferson Pastuña-Fasso[1], Roberth Reye, Katterine Olalla-Tacuri[1], José R. Almeida[1], Melanie Ochoa-Ocampo[1], Pablo Cisneros-Pérez[3], Patricio J. Espinoza-Montero[2*]

[1] Biomolecules Discovery Group, Universidad Regional Amazónica Ikiam, Tena 150102, Ecuador.

[2] Facultad de Ciencias Exactas, Naturales y Ambientales, Pontificia Universidad Católica del Ecuador, Quito 170525, Ecuador.

[3] Yachay Tech University, School of Chemical Sciences and Engineering, Urcuqui 100650, Ecuador.

*E-mail address: pespinoza646@puce.edu.ec (Patricio J. Espinoza-Montero)

+ These authors contributed equally

Abstract

Diabetes-associated oxidative stress and accelerated postprandial carbohydrate digestion are complementary therapeutic targets that motivate the identification of multifunctional plant metabolites. Here we integrated phytochemical profiling, bioactivity assays and *in silico* analyses to characterize peel, pulp and seed extracts from *Oenocarpus bataua* Mart., an Amazonian palm. Seed extracts exhibited the highest total phenolic content (2250.8 mg GAE/100 g dw) and pronounced antioxidant capacity (DPPH IC_{50} = 17.0 µg/mL; ABTS IC_{50} = 20.1 µg/mL; FRAP = 485.5 µmol Fe^{2+}/g dw), whereas pulp showed intermediate responses. Potent α-amylase inhibition was observed for pulp and seed extracts (IC_{50} = 3.93 and 3.47 µg/mL), surpassing acarbose, while α-glucosidase inhibition was strongest in pulp and peel. UPLC–ESI–QTOF–MS/MS annotated procyanidins (B1–B3, C1), catechins and flavonoid glycosides. Molecular docking identified procyanidin B2 (ΔG ≈ −10.1 kcal/mol) as a high-affinity ligand for digestive enzymes, and ADMET screening supported its prioritization. These findings define tissue-specific bioactivities and highlight pulp and seed as promising sources of glycemia-modulating phytochemicals.

Keywords: antidiabetic, secondary metabolites, antioxidant activity, molecular docking, ADMET

Diabetes mellitus is a complex, multifactorial metabolic disorder and represents one of the most significant global public health challenges. It is characterized by chronic hyperglycemia resulting from impaired insulin secretion, defective insulin action, or a combination of both mechanisms. In autoimmune forms, T-cell–mediated immune responses progressively destroy insulin-producing pancreatic β-cells, ultimately leading to absolute insulin deficiency. In addition, modifiable lifestyle factors, including physical inactivity and unhealthy dietary patterns, substantially contribute to disease onset and progression. Current estimates indicate that diabetes affects more than 430 million individuals worldwide, and its prevalence continues to increase at an alarming rate[1]. The management of postprandial hyperglycemia constitutes a central therapeutic objective in diabetes care. Enzymes involved in carbohydrate digestion, particularly α-amylase and α-glucosidase, are well-established pharmacological targets, as their inhibition delays glucose release and intestinal absorption, thereby attenuating postprandial glucose excursions. Several synthetic inhibitors, such as metformin, sulfonylureas, acarbose, miglitol, voglibose, and emiglitate, are widely used in clinical practice. Although effective, these agents are frequently associated with gastrointestinal adverse effects and limited target specificity[2]. These limitations have driven increasing interest in plant-derived bioactive compounds as safer or complementary therapeutic alternatives. Natural products often exhibit multifunctional properties, including concurrent enzyme-inhibitory and antioxidant activities. This dual mechanism is particularly relevant in the context of diabetes, where oxidative stress plays a pivotal role in disease progression and the development of complications[3-5]. Collectively, these findings support the exploration of phytochemicals as promising candidates for the development of novel antidiabetic strategies.

Plants constitute an exceptional source of chemically diverse specialized metabolites, shaped by evolutionary adaptation to specific biotic and abiotic pressures. Individual species may biosynthesize thousands of structurally distinct compounds, collectively contributing to an extensive global chemodiversity[6]. This vast metabolic diversity underpins the continued exploration of plant-derived compounds for pharmaceutical and nutraceutical applications.

The Amazon rainforest represents one of the most important reservoirs of pharmacologically active plant species, many of which remain insufficiently characterized. Among these, *Oenocarpus bataua* Mart. (Arecaceae), commonly known as Patawa, Seje, Chapil, or Ungurahua, is a palm species native to the Amazonian regions of Ecuador, Colombia, Brazil,

and Panama. The species can reach heights of up to 25 m and produces approximately 1,200–2,200 purple, ovoid fruits per tree annually. Traditionally, it has been used as a botanical supplement and in ethnomedicine, particularly for its antioxidant and antimalarial properties[7].

Phytochemical investigations have revealed that *O. bataua* fruits are rich in phenolic compounds, including anthocyanins, tannins, and stilbenes[7-9]. Given the well-documented association between phenolic constituents and bioactivities such as enzyme inhibition and oxidative stress modulation, these findings suggest that *O. bataua* represents a promising candidate for further investigation in the context of metabolic disorder management.

Despite its recognized ethnopharmacological relevance and well-documented phytochemical richness, the antidiabetic potential of *Oenocarpus bataua*, particularly with respect to digestive enzyme inhibition, remains insufficiently explored. In this context, the present study aimed to evaluate the *in vitro* antioxidant and antidiabetic activities of *O. bataua* extracts. Specialized metabolites were profiled using ultra-performance liquid chromatography coupled with electrospray ionization quadrupole time-of-flight mass spectrometry (UPLC-ESI-QTOF-MS). The analysis enabled the tentative identification of diverse secondary metabolites, including polyphenols, flavonoids, and phenylpropanoids. Given the established role of carbohydrate-hydrolyzing enzymes in postprandial glucose regulation, selected key metabolites were subsequently subjected to *in silico* molecular docking analyses against human pancreatic α-amylase (PDB ID: 4GQR) and α-glucosidase (PDB ID: 3A4A), both recognized as critical therapeutic targets in diabetes management.

Collectively, these findings provide novel insights into the bioactive profile of *O. bataua* and highlight its potential as a source of structurally diverse natural scaffolds for the development of antidiabetic agents.

Results and discussion

Antioxidant measurements

Dietary phenolic compounds are widely recognized for their pronounced antioxidant properties, which are largely attributed to their structural diversity and redox behavior[10]. In the present study, the total phenolic content (TPC) of *Oenocarpus bataua* Mart. extracts differed significantly among fruit tissues. Seed extracts exhibited the highest TPC (2250.8 ± 0.0 mg

GAE/100 g dw), followed by pulp (967.4 ± 0.6 mg GAE/100 g dw) and peel (199.2 ± 0.7 mg GAE/100 g dw).

In contrast, the total flavonoid content (TFC) followed a distinct distribution pattern (seed > peel > pulp), indicating tissue-specific variation in phenolic subclasses (**Table 1**). These findings suggest that different fruit fractions contribute uniquely to the overall phytochemical profile of *O. bataua*.

Antioxidant activity was assessed using DPPH, ABTS, and FRAP assays. All extracts demonstrated concentration-dependent radical scavenging activity. Consistently, seed extracts exhibited the strongest antioxidant potential, with IC_{50} values of 17.0 µg/mL (DPPH) and 20.3 µg/mL (ABTS). This pattern was corroborated by FRAP analysis, in which seed extracts displayed the highest ferric-reducing capacity (485.5 ± 14.4 µmol Fe^{2+}/g dw), followed by pulp (316.2 ± 13.2 µmol Fe^{2+}/g dw) and peel (37.3 ± 0.7 µmol Fe^{2+}/g dw) (**Table 1**).

Collectively, these results indicate that the seed fraction of *O. bataua* represents the most potent source of antioxidant constituents among the evaluated tissues, likely reflecting its elevated phenolic content.

Table 1 | Total phenolic content (TPC), total flavonoid content (TFC), and antioxidant capacity of *O. bataua* Mart. extracts determined by DPPH, ABTS, and FRAP assays

	TFC (QE mg/100 g dw)	**TPC (mg/100 g dw)**	**DPPH (IC_{50} µg/mL)**	**ABTS (IC_{50} µg/mL)**	**FRAP (µmol E Fe^{2+}/g dw)**
Peel	6.9 ± 0.20^{a}	199.20 ± 0.70^{c}	246.60 ± 6.7^{a}	222.40 ± 1.60^{a}	37.30 ± 0.70^{c}
Pulp	4.42 ± 0.02^{c}	967.40 ± 0.60^{b}	29.80 ± 0.3^{b}	40.80 ± 0.40^{b}	316.20 ± 13.20^{b}
Seed	5.35 ± 0.04^{b}	2250.8 ± 0.00^{a}	17.00 ± 0.3^{c}	20.10 ± 0.20^{c}	485.50 ± 14.40^{a}

Values are expressed as mean ± standard deviation (n = 3). Different letters within the same column indicate significant differences according to one-way ANOVA followed by Tukey's HSD post hoc test ($p < 0.05$).

Seed extracts of *Oenocarpus bataua* Mart. contained markedly higher levels of total phenolics (TPC: 2250.8 mg GAE/100 g dw) and total flavonoids (TFC) compared with pulp (967.4 mg GAE/100 g dw) and peel (199.2 mg GAE/100 g dw). These differences were statistically significant, as determined by one-way ANOVA followed by Tukey's HSD post hoc test ($p < 0.05$). The enrichment of phenolic compounds in seeds relative to other fruit tissues is consistent

with previous reports in other species. For example, grape seeds have been shown to contain TPC values ranging from 15,156 to 48,125 mg GAE/100 g dw, whereas grape pulp contains only 211–268 mg GAE/100 g dw, representing a difference exceeding 130-fold[11].

Pearson correlation analysis further demonstrated strong associations between phenolic composition, antioxidant capacity, and enzyme inhibitory activities (**Fig. 1**). TPC exhibited strong positive correlations with FRAP ($r = 0.96$), DPPH ($r = 0.81$), and ABTS ($r = 0.84$) values, indicating that phenolic constituents are major contributors to the antioxidant potential of *O. bataua* extracts. These findings support the hypothesis that phenolic enrichment, particularly in seed tissues, underpins the observed bioactivities.

Similarly, α-amylase inhibitory activity was strongly and positively correlated with antioxidant capacity, as reflected by DPPH ($r = 1.00$), ABTS ($r = 1.00$), and FRAP ($r = 0.93$) values. These findings suggest that compounds contributing to radical scavenging and reducing capacity may also play a role in α-amylase inhibition.

In contrast, total flavonoid content (TFC) exhibited moderate to strong negative correlations with most antioxidant assays ($r = -0.72$ to -0.91), indicating that not all flavonoid subclasses equally contribute to the antioxidant responses measured. This observation underscores the structural diversity within flavonoids and the potential influence of specific substitution patterns on redox behavior.

Notably, α-glucosidase inhibition showed a strong negative correlation with TPC ($r = -0.83$) and moderate negative correlations with antioxidant capacity assays, suggesting an inverse relationship between global antioxidant potential and α-glucosidase inhibitory activity in the evaluated extracts. In contrast, α-amylase inhibition demonstrated strong positive associations with TPC and antioxidant parameters.

The divergent correlation patterns observed for α-glucosidase and α-amylase are biologically plausible, given their differences in substrate specificity, catalytic mechanisms, and sensitivity to phenolic structures. While antioxidant-related phenolics may co-vary with or enhance α-amylase inhibitory responses, α-glucosidase inhibition appears to depend on distinct structural features. These findings highlight the complexity of enzyme–phenolic interactions and emphasize that total phenolic abundance alone does not fully predict enzyme-specific inhibitory activity[12].

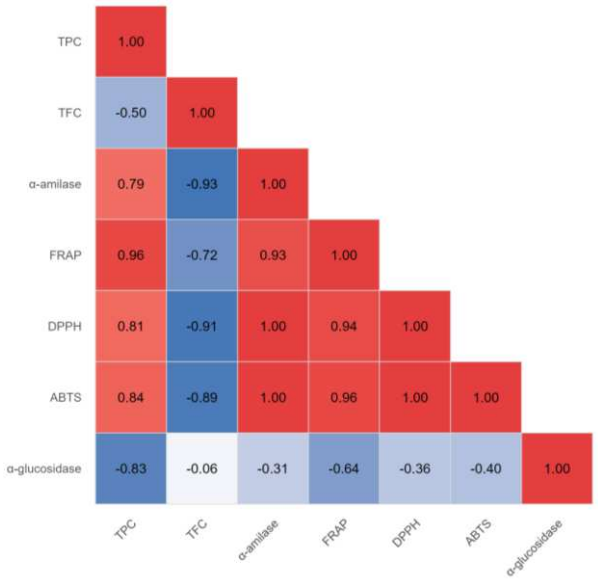

Fig. 1 | Pearson correlation heatmap illustrating the relationships among TPC, TFC, antioxidant capacity assays (DPPH, ABTS, and FRAP), and digestive enzyme inhibitory activities (α-amylase and α-glucosidase). Color intensity represents the strength and direction of the correlation coefficients (r values), with positive correlations shown in warm tones and negative correlations in cool tones. Statistically significant correlations after Benjamini–Hochberg false discovery rate (FDR) correction are indicated accordingly.

In vitro inhibitory activity of carbohydrate metabolizing enzymes by plant extract

A broad spectrum of specialized plant metabolites has been reported to contribute to diabetes management due to their structural diversity and capacity to modulate key metabolic targets, including carbohydrate-hydrolyzing enzymes such as α-amylase and α-glucosidase. In the present study, ethanolic extracts obtained from the peel, pulp, and seed of *Oenocarpus bataua* Mart. were evaluated for their *in vitro* inhibitory activity against both enzymes.

As summarized in Table 2, substantial differences in inhibitory potency were observed among fruit fractions and between the two enzymes. Regarding α-amylase inhibition, pulp and seed extracts exhibited the strongest activities, with IC_{50} values of 3.93 ± 0.05 µg/mL and 3.47 ± 0.03 µg/mL, respectively. No statistically significant difference was detected between these two extracts ($p > 0.05$). Notably, both fractions demonstrated significantly greater inhibitory potency than the reference drug acarbose (IC_{50} = 16.55 ± 1.76 µg/mL). In contrast, the peel extract showed markedly lower activity, with an IC_{50} value of 398.07 ± 11.14 µg/mL.

These findings indicate that the pulp and seed fractions of *O. bataua* are particularly enriched in bioactive constituents capable of effectively inhibiting α-amylase, highlighting their potential relevance for modulating postprandial glucose metabolism.

In contrast to the α-amylase results, a distinct inhibition pattern was observed for α-glucosidase. The pulp extract exhibited the strongest inhibitory activity (IC_{50} = 14.98 ± 0.05 µg/mL), followed by the peel extract (IC_{50} = 20.26 ± 0.05 µg/mL), whereas the seed extract showed comparatively lower activity (IC_{50} = 39.51 ± 0.05 µg/mL). Under the experimental conditions employed, acarbose demonstrated weaker α-glucosidase inhibition (IC_{50} = 56.87 ± 3.49 µg/mL), underscoring the pronounced and enzyme-specific inhibitory potential of the *O. bataua* extracts.

The contrasting inhibition profiles observed for α-amylase and α-glucosidase are consistent with the Pearson correlation analysis and suggest that distinct classes of phytochemicals are involved in modulating each enzyme. Whereas α-amylase inhibition appears to be closely associated with phenolic-rich fractions, α-glucosidase inhibition may depend on alternative structural features, such as compound polarity, molecular size, or specific functional groups. This differential behavior further supports the concept that antioxidant capacity and digestive enzyme inhibition are not necessarily governed by the same chemical determinants[12]. Overall, the strong α-amylase inhibition exhibited by pulp and seed extracts, together with the effective α-glucosidase inhibition particularly observed in the pulp fraction, highlights the potential of *O. bataua* as a promising source of bioactive compounds for the development of functional foods or nutraceutical formulations aimed at glycemic control.

Table 2 | *In vitro* α-amylase and α-glucosidase inhibitory activities of *Oenocarpus bataua* Mart. peel, pulp, and seed extracts, expressed as IC_{50} values (µg/mL)

	IC_{50} (µg/mL) α-amylase	IC_{50} (µg/mL) α-glucosidase
Peel	398.07 ± 11.14[a]	20.26 ± 0.05[c]
Pulp	3.93 ± 0.05[b]	14.98 ± 0.05[d]
Seed	3.47 ± 0.03[b]	39.51 ± 0.05[b]
Acarbose	16.55 ± 1.76[c]	56.87 ± 3.49[a]

Values are expressed as mean ± standard deviation (n = 3). Different letters within the same column indicate significant differences according to one-way ANOVA followed by Tukey's HSD post hoc test ($p < 0.05$).

Metabolomic profile

Table 3 presents the components identified in by LC-MS/MS organized according to ionization mode and collision energy: 10 eV (+) (GNPS – 10 eV (ID = ecee3bbec41f47549b068b8f63f6b532)), 20 eV (+) (GNPS – 20 eV)(ID = 19ce51c9db5b418fabcff803435207de), 10 eV (−) (GNPS – 10 eV (ID= 85c507864b9b464a9f607e05bce854e9)), and 20 eV (−) (GNPS – 20 eV(ID= 4d5f30d446484533ad01c816a5c1ffd2)). A total of 2 compounds were identified at level 1, 37 at level 2, and 2 at level 3. The classification into putative chemical classes was based on spectral matches against public MS/MS libraries.

Table 3 | Compounds identified in hydroethanolic extracts of *Oenocarpus bataua* Mart. using UPLC-MS/MS

IL	Rt (min)	$[M-H]^-$	$[M-H]^+$	Molecular Formula	Error ppm	MS2 Score	Identification	Metabolite classification
2	3.360	353.087	-	$C_{16}H_{18}O_9$	-2.20	0.95	Chlorogenic acid	Organic oxygen compounds
1	0.535	175.024	-	$C_6H_8O_6$	2.80	-	Ascorbic acid	Organic oxygen compounds
1	3.354	227.070	-	$C_{14}H_{12}O_3$	1.79	-	Transresveratrol	Phenylpropanoids and polyketides
2	0.852	173.044	-	$C_7H_{10}O_5$	-8.80	0.87	Shikimic acid	Organic oxygen compounds
2	3.485	289.072	-	$C_{15}H_{14}O_6$	-2.50	0.86	Epicatechin	Phenylpropanoids and polyketides
2	3.490	577.135	-	$C_{30}H_{26}O_{12}$	-0.20	0.83	Procyanidin B1	Phenylpropanoids and polyketides
2	3.377	577.135	-	$C_{30}H_{26}O_{12}$	-0.20	0.81	Procyanidin B2	Phenylpropanoids and polyketides
2	4.505	243.065	-	$C_{14}H_{12}O_4$	-5.70	0.78	E-Piceatannol	Phenylpropanoids and polyketides
2	6.285	329.231	-	$C_{18}H_{34}O_5$	-0.98	0.75	FA 18:1+3O	Lipids and lipid-like molecules
2	3.665	289.071	-	$C_{15}H_{14}O_6$	-2.50	0.95	Catechin	Phenylpropanoids and polyketides
2	1.053	191.019	-	$C_6H_8O_7$	-3.60	0.93	Citric acid	Organic acids and derivatives

2	3.008	-	146.061	C_9H_7NO	6.41	0.97	1H-Indole-4-carboxaldehyde	Phenylpropanoids and polyketides
2	0.901	-	124.040	C_6H_5NO2	5.41	0.78	Niacin	Organoheterocyclic compounds
2	5.869	-	273.076	$C_{15}H_{12}O_5$	1.09	0.97	Naringenin	Phenylpropanoids and polyketides
2	3.010	-	205.098	$C_{11}H_{12}N_2O_2$	4.00	0.95	D-Trytophan	Organoheterocyclic compounds
2	2.480	-	166.087	$C_9H_{11}NO_2$	4.34	0.96	Phenylalanine	Organic acids and derivatives
2	0.565	-	182.082	$C_9H_{11}NO_3$	4.43	0.95	Tyrosine	Organic acids and derivatives
2	2.199	-	284.1	$C_{10}H_{13}N_5O_5$	3.66	0.95	Guanosine	Organic nitrogen compounds
2	3.691	-	579.154	$C_{30}H_{26}O_{12}$	7.37	0.95	Procyanidin B3	Phenylpropanoids and polyketides
2	3.296	-	595.167	$C_{27}H_{30}O_{15}$	2.18	0.93	kaempferol-3-O-robinobioside	Phenylpropanoids and polyketides
2	0.574	-	118.087	$C_8H_{19}NO_2$	6.11	0.92	Betaine	Organic acids and derivatives
2	4.485	-	245.082	$C_{14}H_{12}O_4$	4.65	0.92	Piceatannol	Phenylpropanoids and polyketides
2	3.740	-	565.156	$C_{26}H_{28}O_{14}$	1.40	0.90	Isoschaftoside	Phenylpropanoids and polyketides
2	3.818		565.156	$C_{26}H_{28}O_{14}$	1.40	0.88	Corymboside	Phenylpropanoids and polyketides
2	4.565	-	317.067	$C_{16}H_{12}O_7$	4.40	0.88	Quercetin 3'-methyl ether	Phenylpropanoids and polyketides
2	9.061	-	454.293	$C_{16}H_{31}NO_4P$	0.37	0.88	PE(16:0/0:0)	Lipids and lipid-like molecules
2	3.689	-	867.213	$C_{45}H_{38}O_{18}$	-0.13	0.92	Procyanidin C1	Phenylpropanoids and polyketides
2	4.240	-	303.051	$C_{15}H_{10}O_7$	3.45	0.87	3,7,3',4',5'-Pentahydroxyflavone	Phenylpropanoids and polyketides
2	10.11	-	357.3	$C_{21}H_{40}O_4$	0.11	0.87	Monoolein	Lipids and lipid-like molecules

2	6.028	-	331.082	$C_{17}H_{14}O_7$	2.25	0.84	Tricin	Phenylpropanoids and polyketides
2	11.921	-	593.276	$C_{35}H_{36}N_4O_5$	0.21	0.83	Pheophorbide A	Organoheterocyclic compounds
2	5.904	-	271.061	$C_{15}H_{10}O_5$	3.24	0.82	Apigenin	Phenylpropanoids and polyketides
2	8.489	-	359.114	$C_{19}H_{18}O_7$	4.03	0.82	3'-Hydroxy-5,6,7,4'-tetramethoxyflavone	Phenylpropanoids and polyketides
3	7.403	-	339.232	$C_{20}H_{18}O_5$	-	0.81	Licoflavone C	Phenylpropanoids and polyketides
2	9.388	-	277.217/[M+H-H_20]$^+$	$C_{18}H_{30}O_3$	2.78	0.79	9S-Hydroxy-10E,12Z,15Z-octadecatrienoic acid	Lipids and lipid-like molecules
2	3.657	-	139.04	$C_7H_6O_3$	7.23	0.75	Salicylic acid	Benzenoids
2	4.425	-	479.119	$C_{22}H_{22}O_{12}$	1.19	0.73	Isorhamnetin-3-glucoside	Phenylpropanoids and polyketides
3	4.406	-	177.113/[M+Na]$^+$	$C_{10}H_{18}O$	-	0.73	Geraniol	Lipids and lipid-like molecules
2	7.930	-	295.228	$C_{18}H_{30}O_3$	4.08	0.72	13-Keto-9Z,11E-octadecadienoic acid	Lipids and lipid-like molecules
2	4.154	-	433.133	$C_{21}H_{20}O_{10}$	0.12	0.84	3-Genistein-8-C-glucoside	Phenylpropanoids and polyketides
2	0.557	-	138.056	$C_7H_7NO_2$	7.39	0.75	Trigonelline	Organoheterocyclic compounds

IL, identification level according to Summer et al. (2007); RT, retention time in minutes; MS2 score for level 2 identification refers to GNPS modified cosine score

Additionally, principal component analysis (PCA) and hierarchical clustering heatmaps were employed to investigate metabolomic relationships among the different anatomical parts of *O. bataua* Mart. (**Fig. 2**).

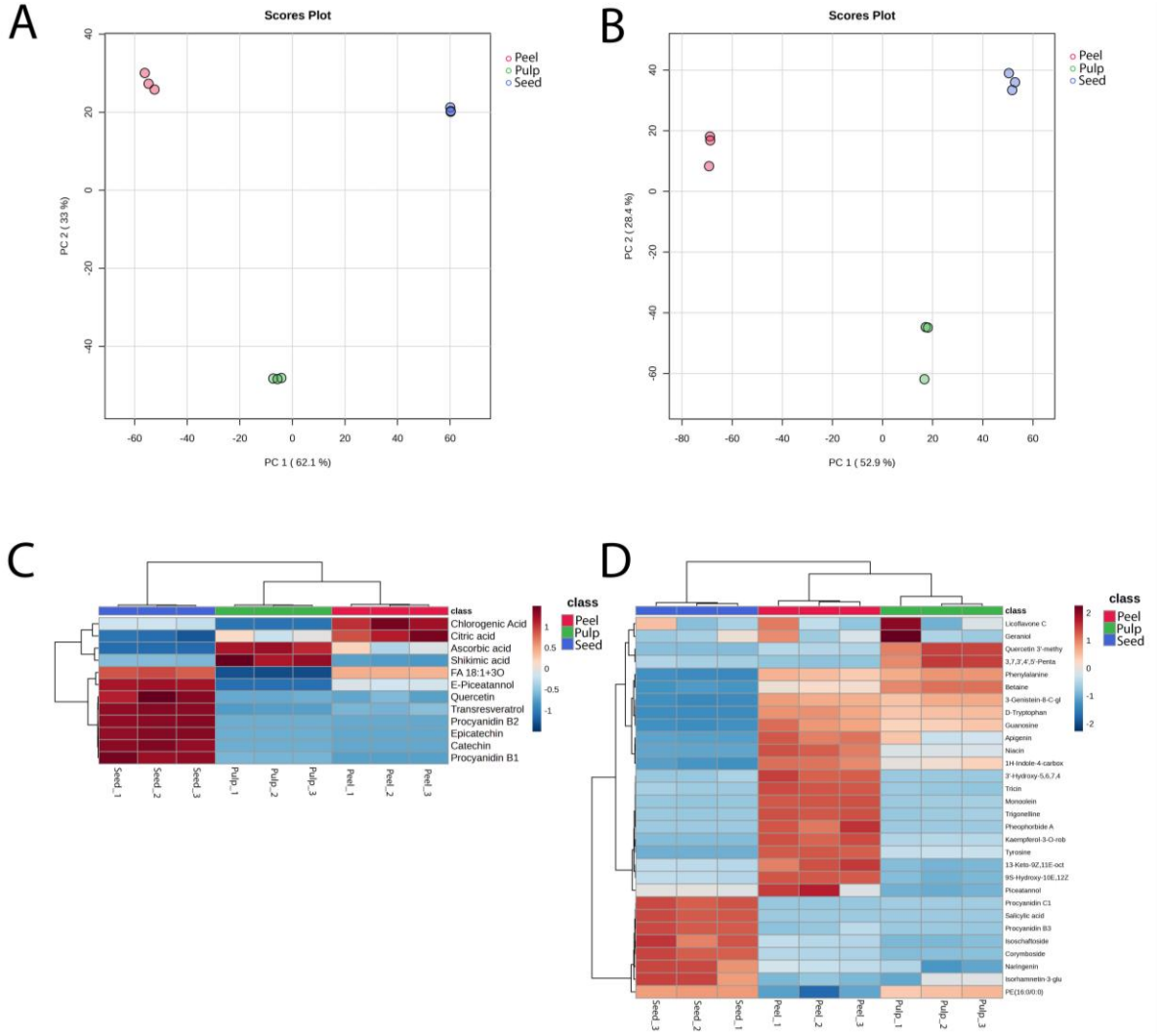

211

212 **Fig. 2 | Multivariate analysis of LC–MS metabolomic profiles of *Oenocarpus bataua* Mart.**
213 **extracts.** (A) Score plot obtained in negative ionization mode. (B) Score plot obtained in positive
214 ionization mode. (C) Heatmap coupled with HCA in negative ionization mode. (D) Heatmap coupled
215 with HCA in positive ionization mode. Score plots illustrate sample clustering patterns based on
216 metabolite profiles, while heatmaps and HCA depict relative metabolite abundance and similarity
217 relationships among peel, pulp, and seed extracts.

218 PCA of the LC–MS metabolomic dataset revealed pronounced tissue-specific metabolic
219 differentiation in both negative and positive ionization modes. In negative ion mode, principal
220 component 1 (PC1) explained 62.1% of the total variance (**Fig. 2A**), whereas in positive ion
221 mode, PC1 accounted for 52.9% (**Fig. 2B**). The clear separation along PC1 indicates that tissue
222 type represents the primary source of metabolic variation. In both ionization modes, peel
223 samples clustered within the negative PC1 region, seed samples were consistently positioned

in the positive PC1 region, and pulp samples were located near the origin (negative mode) or slightly shifted toward positive PC1 values (positive mode). These consistent clustering patterns confirm substantial metabolic divergence among peel, pulp, and seed tissues.

To further characterize metabolite distribution patterns, hierarchical cluster analysis (HCA) combined with heatmap visualization was conducted (**Figs. 2C** and **2D**). In negative ionization mode (**Fig. 2C**), HCA delineated three clearly separated clusters corresponding to the three fruit tissues. The peel fraction was characterized by elevated levels of chlorogenic acid and citric acid, metabolites associated with phenolic biosynthesis, primary carbon metabolism, and defense responses to biotic stress[13]. This enrichment aligns with the biological role of the peel as both a structural and biochemical barrier, contributing to protection against environmental and microbial challenges.

Pulp samples were characterized by elevated levels of ascorbic acid and shikimic acid, metabolites closely associated with antioxidant defense and metabolic adjustments during fruit ripening and senescence[14]. Ascorbic acid plays a central role in maintaining redox homeostasis, while shikimic acid is a key intermediate in the biosynthesis of aromatic amino acids and phenolic compounds. The enrichment of these metabolites likely reflects the high metabolic activity of the pulp and its requirement for tight regulation of oxidative balance and membrane stability.

In contrast, seed samples displayed a distinct metabolomic profile enriched in flavonoid-related compounds, including procyanidin B1, catechin, epicatechin, trans-resveratrol, quercetin, and E-piceatannol. These polyphenolic constituents are widely recognized for their potent antioxidant properties and their protective roles in embryonic tissues, contributing to seed dormancy, structural integrity, and longevity[15,16]. The pronounced accumulation of these compounds in seeds is consistent with their physiological function in safeguarding genetic material against oxidative and environmental stress.

In positive ionization mode (**Fig. 2D**), hierarchical clustering analysis identified three clearly separated metabolite groups corresponding to tissue-specific enrichment patterns. The first cluster comprised compounds predominantly enriched in the pulp, present to a lesser extent in the peel, and nearly absent in the seed. These included licoflavone C, geraniol, quercetin 3′-methyl ether, and 3,7,3′,4′,5′-pentahydroxyflavone. Such metabolites, encompassing flavonoids

and a monoterpenoid, are associated with antioxidant defense, aroma biosynthesis, and fruit–environment interactions. They contribute to flavour development and may facilitate the attraction of seed dispersers. Flavonoid derivatives, including methylated quercetin forms and highly hydroxylated flavones, are also implicated in stress-response pathways and ripening-associated metabolism, supporting cellular protection and metabolic stability during fruit maturation[17].

A second cluster was dominated by peel-specific metabolites, such as kaempferol-3-O-rutinoside, trigonelline monoalin, piceatannol, and 13-keto-9Z,11E-octadecadienoic acid. These compounds are functionally linked to ultraviolet (UV) protection, antimicrobial defense, and lipid-mediated signaling processes, consistent with the peel's ecological role as a protective interface against environmental stressors[18,19].

Seed samples formed a distinct third cluster characterized by the enrichment of specialized metabolites, including phosphatidylethanolamine [PE(16:0/0:0)], isorhamnetin-3-glucoside, procyanidins C1 and B3, corymboside, and salicylic acid. These metabolites are associated with membrane structural integrity, antioxidant protection, immune-related signaling, and the maintenance of seed viability and dormancy [20]. The distinct clustering pattern observed in positive ion mode further corroborates the marked metabolic specialization of *O. bataua* fruit tissues.

Procyanidins, particularly oligomeric forms such as C1 and B3, belong to the class of condensed tannins and are widely recognized for their potent antioxidant properties and protective functions in seeds. These compounds contribute to defense against oxidative damage and microbial attack, thereby supporting seed longevity and viability[21,22]. In parallel, salicylic acid acts as a central phytohormone in plant immune signaling and has been shown to enhance germination under stress conditions by modulating defense-related pathways[23]. The exclusive or predominant enrichment of these metabolites in seed tissue reinforces their functional relevance in seed protection and preparedness for germination.

Collectively, the PCA and HCA results obtained in both ionization modes demonstrate that peel, pulp, and seed tissues of *Oenocarpus bataua* possess clearly differentiated and functionally specialized metabolomic profiles. The peel is characterized by barrier-associated phenolics and defense-related metabolites; the pulp is enriched in antioxidant and ripening-

associated compounds; and the seed accumulates bioactive flavonoids and signaling molecules essential for embryonic protection, dormancy maintenance, and stress resilience. These findings highlight the pronounced metabolic compartmentalization within *O. bataua* fruits and provide a biochemical basis for their distinct biological activities.

Correlation between metabolite profile, antioxidant activity, and enzyme inhibition

The multivariate integration of biological assays with metabolomic data revealed clear tissue-dependent biological behavior among peel, pulp, and seed extracts. The PCA biplot constructed using biological parameters (TPC, TFC, DPPH, ABTS, FRAP, α-amylase, and α-glucosidase inhibition) demonstrated structured separation of fruit tissues and selective alignment of assays with specific matrices (**Fig. 3A**). Total flavonoid content (TFC) was primarily associated with peel samples, whereas total phenolic content (TPC) and ferric reducing antioxidant power (FRAP) were more closely aligned with seed extracts. In contrast, radical scavenging assays (DPPH and ABTS), together with α-amylase inhibition, clustered nearer to pulp samples, indicating that distinct antioxidant mechanisms and bioactive drivers predominate in each tissue.

Integration of the assay-based PCA with the Pearson correlation heatmap linking metabolites and bioactivities (**Fig. 3B**), alongside the abundance heatmaps (**Fig. 2**), enabled identification of compound classes underpinning specific biological responses. Antioxidant-related assays (DPPH, ABTS, and FRAP), as well as TPC, exhibited strong positive correlations ($r > 0.7$) with phenolic families, including flavan-3-ols, proanthocyanidins, stilbenes, and stilbenoids. These classes are widely recognized for their electron-donating capacity and metal-reducing properties, which mechanistically explains their close association with reducing power and radical scavenging assays.

By contrast, α-amylase inhibition showed weaker and more variable correlations with these phenolic groups, suggesting that inhibitory activity is not governed solely by overall phenolic abundance but may depend on specific structural features, such as hydroxylation patterns, degree of polymerization, or molecular conformation. These findings emphasize the importance of structural selectivity in enzyme–ligand interactions and further support the notion that

antioxidant capacity and digestive enzyme inhibition are mediated by partially distinct chemical determinants.

At the individual metabolite level, isorhamnetin-3-glucoside emerged as the compound exhibiting the most consistent positive correlations with antioxidant capacity parameters, TPC, and α-amylase inhibition. This pattern suggests that certain glycosylated flavonols may simultaneously contribute to redox activity and enzyme interaction. In contrast, α-glucosidase inhibition displayed strong negative correlations with condensed phenolic groups and proanthocyanidin-enriched profiles. This inverse relationship indicates that high-molecular-weight and polymeric phenolics may be particularly effective in modulating α-glucosidase activity, potentially through mechanisms involving protein precipitation, non-specific binding, or steric blocking of catalytic sites.

Several metabolites identified as statistically significant contributors—including isoschaftoside, corymboside, and naringenin—further support the involvement of both flavonoid glycosides and flavan-3-ol derivatives in shaping the observed inhibition patterns. Collectively, these findings support a model in which enzyme inhibition arises from the combined influence of phenolic density, degree of polymerization, and glycosylation pattern, rather than from a single dominant compound class.

When these correlation patterns are examined alongside metabolite abundance heatmaps, a coherent tissue-dependent interpretation becomes evident. Seed extracts, which cluster with TPC and FRAP in the PCA biplot (**Fig. 3A**), exhibit elevated relative abundances of procyanidins (B1, B2, B3, and C1), catechin, epicatechin, trans-resveratrol, and E-piceatannol (**Figs. 3C** and **3D**). These metabolites show strong positive correlations with TPC, FRAP, DPPH, ABTS, and α-amylase inhibition, supporting their role as principal contributors to the high reducing power and phenolic content observed in seed extracts[21].

In parallel, these same phenolic constituents exhibited strong negative correlations with α-glucosidase activity. Their condensed structures and high density of hydroxyl groups favor electron transfer and radical stabilization, which explains their pronounced antioxidant signatures. At the same time, the negative correlation with α-glucosidase activity—consistent with the PCA biplot positioning of α-glucosidase opposite the seed cluster—indicates an

inverse functional association between this enzymatic parameter and the seed-specific phenolic profile.

This spatial separation in the multivariate model supports the interpretation that the phenolic-rich seed metabolome is closely linked to enhanced α-glucosidase inhibition. Mechanistically, condensed tannins and procyanidins are known to interact strongly with carbohydrate-digesting enzymes through hydrophobic interactions and hydrogen bonding, potentially leading to conformational changes or active-site blocking. The consistent opposition between α-glucosidase and seed extracts in the PCA biplot (**Fig. 3A**) further reinforces this inverse relationship, highlighting the selective contribution of seed-derived polyphenols to α-glucosidase inhibitory activity.

Pulp samples clustered in the PCA biplot proximal to DPPH, ABTS, and α-amylase inhibition (**Fig. 3A**), reflecting a distinct metabolomic signature enriched in relatively polar, medium-molecular-weight metabolites[14]. These included ascorbic acid, shikimic acid, selected glycosylated flavonoids, and various organic acids.

These compounds exhibited strong positive correlations with radical-scavenging assays, accounting for the pronounced DPPH and ABTS activities observed in pulp extracts. In contrast, their contribution to ferric reducing antioxidant power (FRAP) was comparatively moderate, consistent with their chemical properties. Many of these metabolites function more efficiently as hydrogen atom donors than as metal-reducing agents, which may explain the differential antioxidant responses across assays.

In addition, their polarity and conformational flexibility may facilitate interaction with α-amylase through surface-level binding and transient complex formation, aligning with the experimentally observed inhibitory activity. Collectively, these findings suggest that pulp bioactivity is predominantly driven by small, polar antioxidants and rapid radical-quenching molecules rather than by highly polymerized condensed phenolics[12].

Peel samples clustered predominantly with total flavonoid content (TFC) in the PCA biplot, reflecting their enrichment in flavonoid glycosides such as kaempferol-3-O-robinobioside, isoschaftoside, corymboside, and quercetin derivatives. These compounds contribute substantially to the overall flavonoid quantification measured in this tissue.

However, their correlations with antioxidant capacity assays were comparatively weaker than those observed for condensed phenolics, such as procyanidins and flavan-3-ols. This difference may be attributed to structural features, including glycosylation patterns and lower degrees of polymerization, which can modulate electron-donating efficiency and radical stabilization capacity[24]. Consequently, although peel extracts are flavonoid-rich, their contribution to overall antioxidant performance appears to be qualitatively distinct from that of the phenolic profiles characterizing seed tissues.

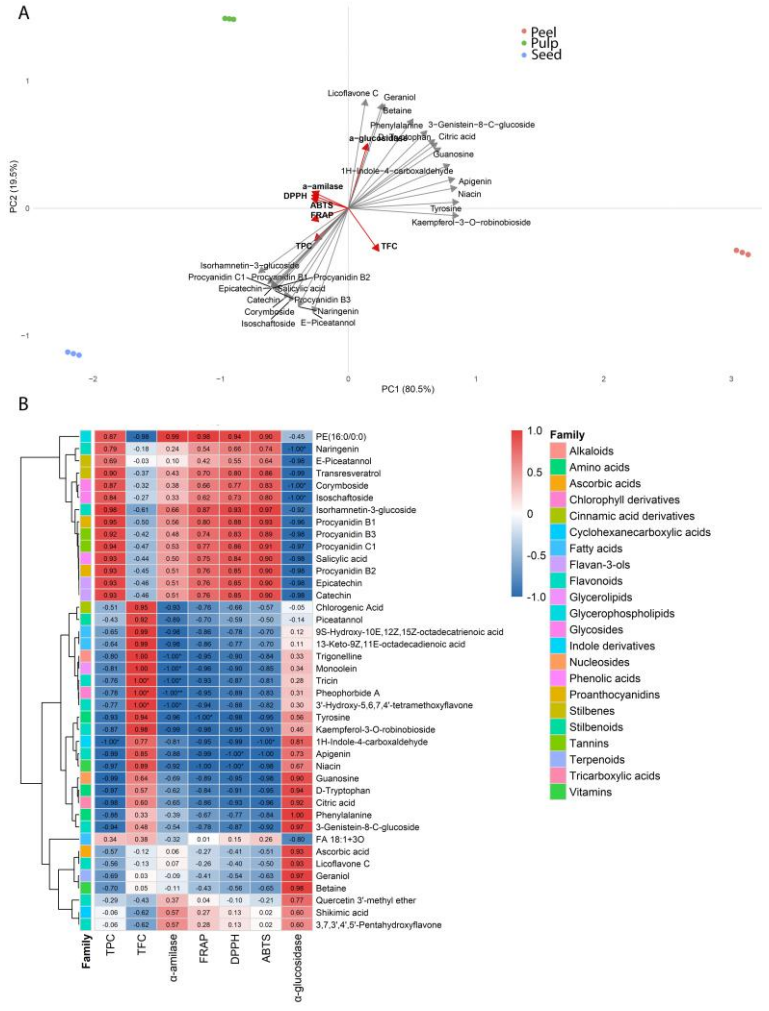

Fig. 3 | Integrated multivariate analysis linking metabolomic features with biological activities in *Oenocarpus bataua* Mart. extracts. **(A)** Principal component analysis (PCA) biplot constructed from biological parameters (TPC, TFC, DPPH, ABTS, FRAP, α-amylase, and α-glucosidase), illustrating tissue-specific clustering and variable associations. **(B)** Pearson correlation heatmap displaying relationships between annotated metabolites and biological activities, with color gradients indicating the direction and magnitude of correlation coefficients.

Molecular Docking of Bioactive Compounds with Human Pancreatic α-amylase and α-glucosidase

Molecular docking was conducted for forty metabolites identified in hydroethanolic extracts of *Oenocarpus bataua* Mart., targeting human pancreatic α-amylase (PDB: 4GQR) and α-glucosidase (PDB: 3A4A) (**Table 4**). This dual-enzyme strategy was implemented to better approximate the coordinated inhibition of carbohydrate digestion. Predicted binding affinities spanned a broad energetic window, ranging from –3.6 to –9.8 kcal/mol for α-amylase and –4.0 to –11.2 kcal/mol for α-glucosidase, reflecting diverse interaction strengths among structurally distinct metabolites.

To prioritize biologically meaningful candidates, compounds were ranked according to their average binding energies across both enzymes. The ten metabolites with the most favorable mean ΔG values were selected for detailed interaction analysis, while complete docking data are provided in **Supplementary Table 1**. As an internal control, redocking was performed using acarbose, a clinically established inhibitor, confirming the reliability of the docking protocol and enabling comparative interpretation of ligand affinities.

Table 4 | Summary of molecular docking results showing binding affinities (kcal/mol) and key ligand–protein interactions of selected metabolites with human pancreatic α-amylase (PDB ID: 4GQR) and α-glucosidase (PDB ID: 3A4A)

Ligand	Affinity (kcal/mol) α-amylase	Interactions_amylase (4GQR)	Affinity (kcal/mol) α-glucosidase	Interactions_glucosidase (3A4A)	Affinity Mean (kcal/mol)
Procyanidin B2	-9	Conventional H-bond: Arg195. π–Anion: Asp300. π–Sigma: Glu233. π–Alkyl: Ala198, Ile235, Leu165. Van der Waals*: Asp197, Glu233, Tyr62, Trp58, Trp59, His305	-11.2	Conventional H-bond: Ser240, Ser241, Asp242, Pro312, Ser311. π–Cation: His280. π–π Stacked: Tyr158. π–π T-shaped: His280. π–Alkyl: Arg315, Lys156, Leu313. Van der Waals*: Ser157, Phe303, Glu411	-10.1
Isoschaftoside	-8.3	Conventional H-bond: Gln63, His305. C–H bond (Carbon Hydrogen	-11.5	Conventional Hydrogen Bonds: His280, Val308, Phe303, Thr310, Asp242.	-9.9

		Bond): Thr163. π–π Stacked: Trp59, Tyr62. Unfavorable acceptor–acceptor: Thr163. Van der Waals*: Trp58		C–H Bond (Carbon Hydrogen Bond): His280. π–Cation: His280, Arg315. π–Anion: Glu411. π–π Stacked: Phe303. π–π T-shaped: His280. Van der Waals*: Arg442, Asp352, Tyr158, Leu313	
Corymboside	-9.4	Conventional H-bond: His305, Asp356, Asp300. C–H bond (Carbon Hydrogen Bond): Trp59, Asp300. π–π Stacked: Trp59. Van der Waals*: Gln63, Tyr62, Glu233, Arg195, Asp197, Trp58	-10.3	Conventional H-bond: Thr310, Arg442, Asp242. C–H bond (Carbon Hydrogen Bond): His280, Pro312. π–Cation: His280, Arg315. π–Anion: Glu411. π–π Stacked: Phe303. π–π T-shaped: His280. Unfavorable donor–donor: Arg315. Unfavorable acceptor–acceptor: Phe303, Thr306. Van der Waals*: Asp352, Tyr158, Leu313	-9.85
Procyanidin B1	-9.2	Conventional H-bond: Asp197, His305. π–Anion: Asp300. π–π Stacked: Tyr62. Amide–π Stacked: Gly306, Ala307. π–Alkyl: Ile235, Ala307. Unfavorable donor–donor: Arg195. Van der Waals*: Thr163, Trp59, Trp58, Glu233	-10.1	Conventional H-bond: Arg315, Arg442, Ser157, Glu277, Asp352, Glu411. C–H bond (Carbon Hydrogen Bond): Glu411. π–Cation: His280, Arg315. π–Donor Hydrogen Bond: His280, Phe303. π–Anion: Glu277. π–π T-shaped: His280. Van der Waals*: Asp242, Tyr158, Thr310	-9.65
Procyanidin B3	-9.1	Conventional H-bond: His201, Glu233. π–Sigma: Leu162. π–π T-shaped: Tyr151. π–Alkyl: Ala198, Ile235, Leu165. Unfavorable	-9.7	Conventional H-bond: Arg315, Thr310. π–π T-shaped: Tyr158. π–Alkyl: Arg315, Lys156. Unfavorable donor–donor: Gln279, Val308. Van der	-9.4

		acceptor–acceptor: Asp300. Van der Waals*: Asp197, Trp58, Arg195, Trp59, Tyr62, Thr163		Waals*: Glu411, Ser157, Phe303, His280, Asp242	
Pheophorbide A	-9.8	Conventional H-bond: Thr163, Ala198, Asp197. π–Sigma: Leu162, Thr163. π–π Stacked: Tyr151. π–Alkyl/Alkyl: Ala198, Ile235, Leu162. Van der Waals*: Arg195, Tyr62, Asp300, Trp58, Trp59, Gln63	-8.4	Conventional H-bond: His280, Arg442, Gln353, Asp352; C–H bond: Arg442, Glu411; π–Cation: His280, Arg315; π–π Stacked: Phe303; π–π T-shaped: His280; Van der Waals*: Thr310, Glu277, Tyr158, Leu313	-9.1
Procyanidin C1	-9.3	Conventional H-bond: Trp59, Gln63, Val354. π–Anion: Asp356. π–Donor Hydrogen Bond: Trp59. π–Sigma: Leu162, Thr163. π–π T-shaped: His305. π–Alkyl: Pro54. Van der Waals*: Tyr62, Glu233	-8.9	Conventional H-bond: Lys156, His280, Thr310, Asp242, Ser157, Glu411, Leu313; C–H bond: His280; π–Cation: His280, Arg315; π–Anion: Glu411; π–Sigma: Tyr158, Phe314; π–π Stacked: His280; π–Alkyl: Arg315, Pro312; Van der Waals*: Phe303, Asp352, Arg442	-9.1
3-Genistein-8-C-glucoside	-8.6	Conventional H-bond: Arg195, Asp197, Gln63. Van der Waals*: Asp197, Glu233, Tyr62, Trp58	-9.5	Conventional H-bond: Pro312, Ser311. π–Cation: His280. π–π T-shaped: His280. Van der Waals*: Asp242, Leu313, Glu277, Arg315, Tyr158, Thr310, Phe303, Arg442, Asp352	-9.05
Isorhamnetin-3-glucoside	-8.5	Conventional H-bond: Gln63. C–H bond (Carbon Hydrogen Bond): Thr163. π–Sigma: Trp59. π–π Stacked: Trp59, Tyr62.	-9.5	Conventional H-bond: His280, Arg315, Ser240, Thr310, Ser311, Ser304. C–H bond (Carbon Hydrogen Bond): His280, Arg315. π–Cation: His280. π–π	-9

		π–Alkyl: Leu165. Van der Waals*: Asp197, Trp58, Asp300		Stacked: Tyr158. π–π T-shaped: His280. π–Alkyl: Phe303, Arg315, Lys156. Unfavorable donor–donor: Asp242. Unfavorable acceptor–acceptor: Ser304. Van der Waals*: Ser157	
Kaempferol-3-O-robinobioside	-8.4	Conventional H-bond: Thr163, His299, Asp197. π–Sigma: Thr163. π–π T-shaped: Trp59. Unfavorable acceptor–acceptor: Glu233, Asp300. Van der Waals*: His305, Trp58, Gln63, Tyr62, Arg195	-9.5	Conventional H-bond: Lys156, Ser240, Asp242, Leu313. C–H bond (Carbon Hydrogen Bond): Arg315, Pro312. π–Cation: Arg442. π–Anion: Glu411. π–Alkyl: Arg315. Van der Waals*: His280, Thr310, Phe303, Asp352, Glu277, Tyr158	-8.95
Redock/ Acarbose	-7.2	-	-9.1	-	-8.15

Notes: Interactions include hydrogen bonds, hydrophobic contacts, π–π stacking, and other relevant binding features within the catalytic or allosteric sites. *Van der Waals interactions are listed only if they involve critical residues.

Molecular interactions and functional relevance

The predicted binding modes of the top-ranked metabolites toward human pancreatic α-amylase (PDB ID: 4GQR) (**Fig. 4**) revealed a recurrent interaction pattern centered on the catalytic triad Asp197–Glu233–Asp300, which is essential for substrate hydrolysis. Polyphenolic ligands, including procyanidin B2, procyanidin B1, procyanidin B3, and corymboside, consistently established hydrogen bonds and/or π–anion interactions with these catalytic residues. Such interactions suggest potential interference with nucleophilic attack and transition-state stabilization during glycosidic bond cleavage.

These polar contacts were further stabilized by aromatic stacking interactions with Trp59 and Tyr62, residues that line the substrate-binding channel and contribute to hydrophobic anchoring as well as substrate positioning. This combination of catalytic site engagement and channel-blocking interactions supports a mechanism involving both direct catalytic inhibition and steric restriction of substrate access.

Several ligands exhibited hybrid interaction profiles, combining strong catalytic hydrogen bonding with secondary stabilizing contacts. For example, pheophorbide A interacted with Asp197 and Thr163 while forming aromatic contacts with Tyr151, favoring stable accommodation within the catalytic groove. Similarly, isoschaftoside established coordinated polar and π-interactions involving Gln63, His305, Trp59, and Tyr62, facilitating ligand positioning near the entrance of the active pocket.

Even in cases where isolated unfavorable contacts were observed, extensive van der Waals complementarity contributed to overall binding stability. These findings indicate that steric occupation of the catalytic cleft, reinforced by multiple non-covalent interactions, remains energetically favorable and may underlie the strong α-amylase inhibitory activity observed experimentally.

Collectively, these interaction patterns are consistent with a competitive inhibition mechanism in which ligands engage both catalytic carboxylate residues and aromatic amino acids within the substrate-binding channel to impede substrate accommodation. The simultaneous involvement of hydrogen bonding with Asp197, Glu233, and Asp300, together with π–π stacking and hydrophobic interactions involving residues such as Trp59 and Tyr62, supports stable occupation of the catalytic groove.

This convergence of polar contacts, aromatic interactions, and hydrophobic packing is characteristic of polyphenol-mediated enzyme inhibition and aligns with previously described mechanisms for phenolic-rich systems. Accordingly, the docking results support the hypothesis that *Oenocarpus bataua* metabolites act as competitive inhibitors by stabilizing within the active site of α-amylase, thereby reducing catalytic turnover and limiting carbohydrate hydrolysis.

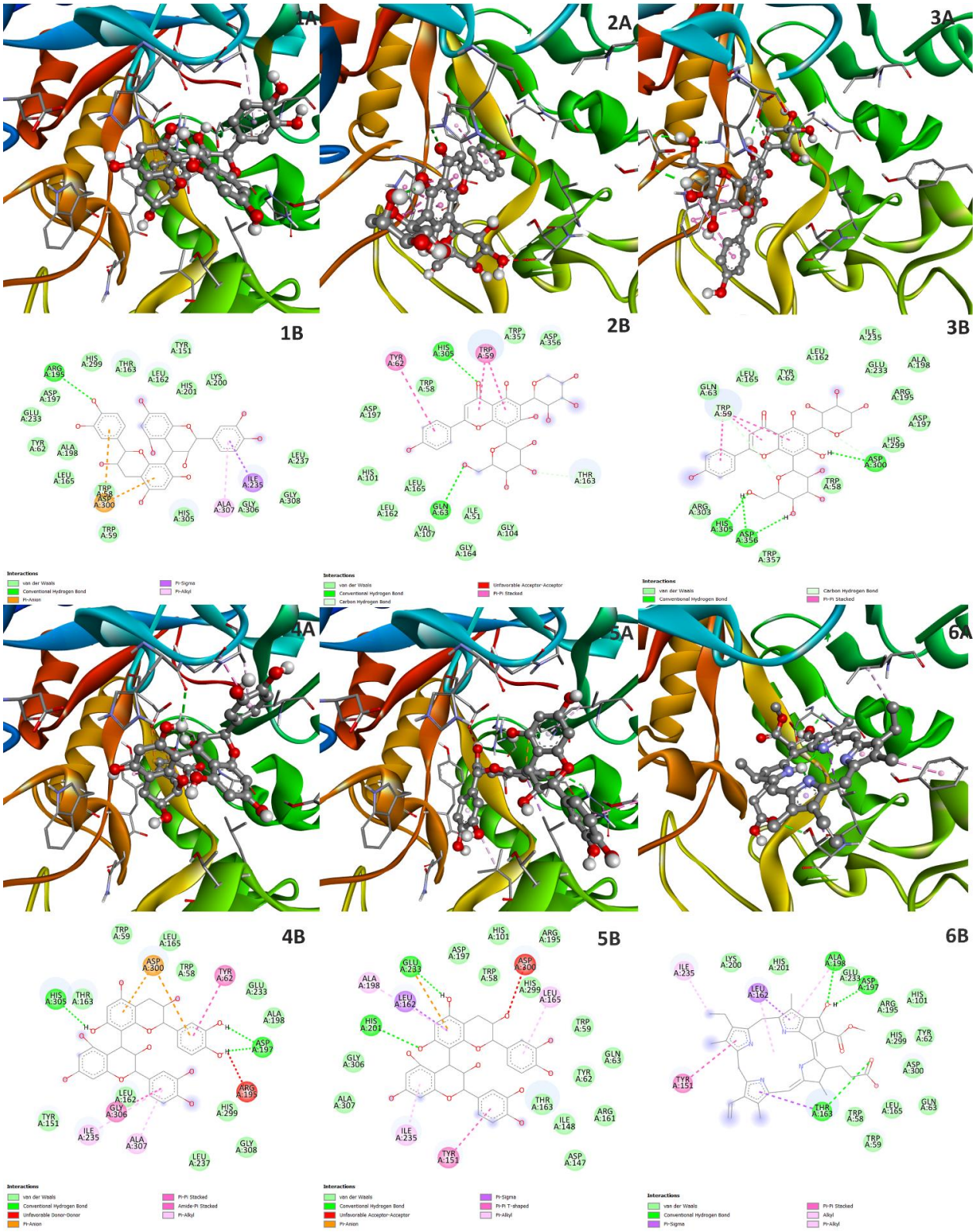

Fig. 4 | Schematic representation of the molecular interactions between selected seed-derived metabolites of *Oenocarpus bataua* and human pancreatic α-amylase (PDB ID: 4GQR). Compounds: (1) Procyanidin B2; (2) Isoschaftoside; (3) Corymboside; (4) Procyanidin B1; (5) Procyanidin B3; (6) Pheophorbide A.

(A) Three-dimensional representation of ligand binding within the catalytic domain (active site) of 4GQR.
(B) Two-dimensional interaction diagrams illustrating hydrogen bonds, π–π stacking, π–anion contacts, and hydrophobic interactions between each ligand and key active-site residues.

The interaction profile within the α-glucosidase active site (PDB ID: 3A4A) (**Fig. 5**) revealed an extensive network of ligand–protein contacts centered on key catalytic residues, including Asp242, Arg315, and His280, which are critical for substrate recognition and glycosidic bond hydrolysis. High-affinity ligands such as procyanidin B2, isoschaftoside, corymboside, and procyanidin B1 formed multiple hydrogen bonds with Asp242 and neighboring polar residues, indicating potential disruption of catalytic geometry and transition-state stabilization. These polar interactions were complemented by π–cation and π–π stacking contacts involving His280 and Tyr158, which contributed to stabilization of the aromatic cores of the ligands within the hydrophobic pocket. The combined presence of catalytic-site hydrogen bonding and aromatic stacking interactions suggests a dual inhibitory mechanism involving both direct interference with catalytic residues and steric occlusion of the substrate-binding cavity. Such interaction patterns are consistent with competitive or mixed-type inhibition and support the experimentally observed α-glucosidase inhibitory activity of *Oenocarpus bataua* metabolites.

Several ligands exhibited multivalent binding behavior typical of extended polyphenolic scaffolds. Procyanidin derivatives, in particular, bridged catalytic and aromatic regions simultaneously through coordinated hydrogen bonding and π-interaction networks, thereby anchoring the ligand firmly within the active pocket. This multivalent interaction pattern enhances binding stability and increases the likelihood of sustained catalytic interference.

Glycosylated flavonoids, such as 3-genistein-8-C-glucoside and isorhamnetin-3-glucoside, preferentially formed hydrogen bonds with peripheral polar residues while preserving aromatic stacking interactions that maintained proximity to the catalytic core. This configuration suggests a balanced binding mode in which glycosyl moieties contribute to polar anchoring, whereas the flavonoid backbone supports hydrophobic and π-mediated stabilization.

Even in cases where suboptimal donor–acceptor geometries were predicted, compensatory hydrophobic contacts and van der Waals interactions contributed to overall binding stability. These findings underscore the importance of cooperative non-covalent interactions in

stabilizing ligand–enzyme complexes and highlight the structural versatility of *Oenocarpus bataua* polyphenols in modulating α-glucosidase activity.

Functionally, the observed interaction pattern supports a competitive inhibition mechanism in which ligands occupy the catalytic cavity and interfere with substrate positioning. Engagement of key catalytic residues through hydrogen bonding, combined with aromatic stabilization within the hydrophobic pocket, is consistent with established structure–activity relationships reported for flavonoid-mediated α-glucosidase inhibition.

The coordinated contribution of polar interactions and π-stacking contacts suggests that these metabolites can effectively stabilize within the active site while perturbing catalytic geometry. Such dual engagement enhances binding affinity and may reduce enzymatic turnover by limiting access of carbohydrate substrates to the catalytic residues.

Overall, these findings indicate that *Oenocarpus bataua* metabolites exhibit sufficient structural versatility to exploit both polar and hydrophobic features of the α-glucosidase active site, supporting their potential to modulate carbohydrate hydrolysis through direct catalytic interference.

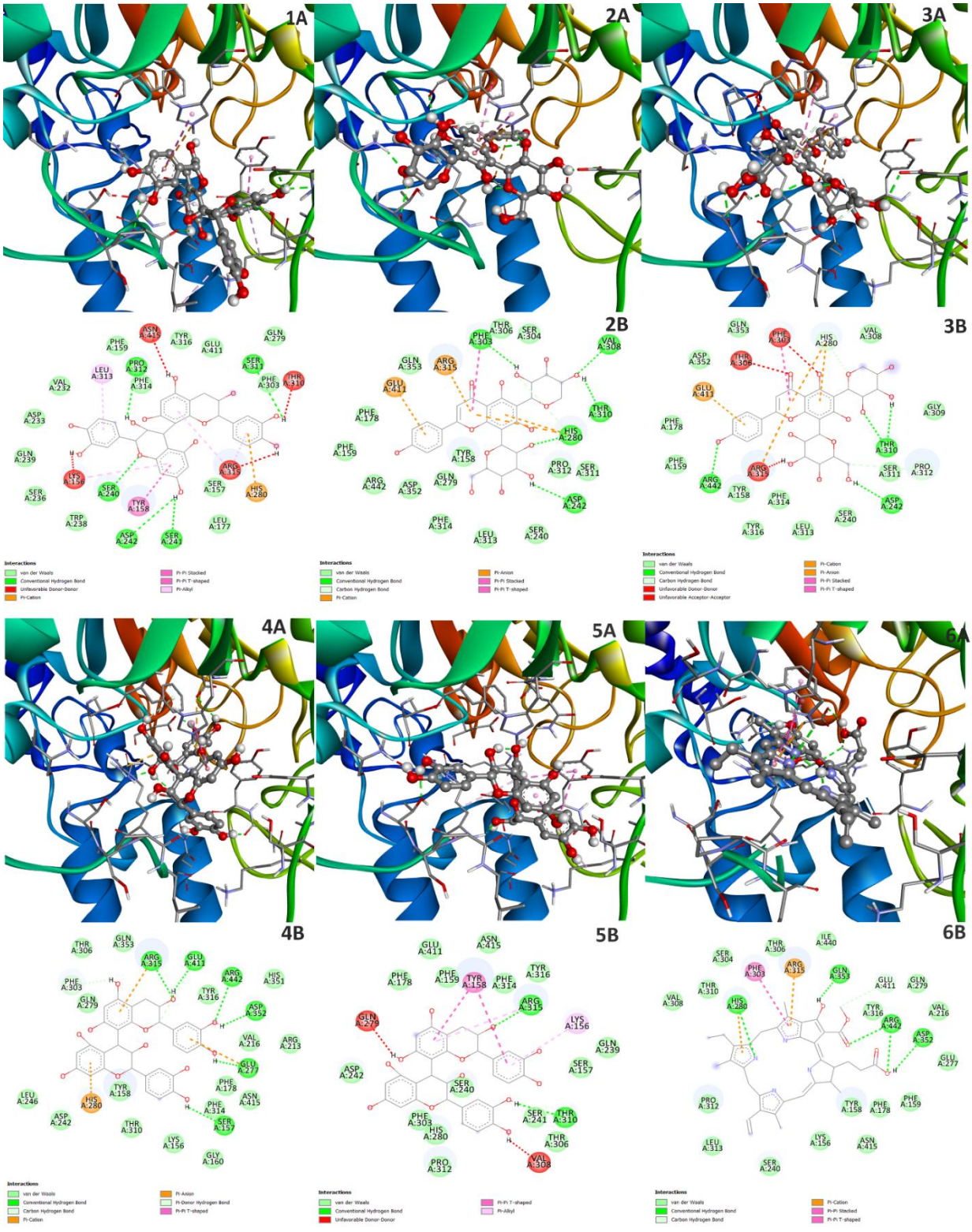

Fig. 5 | Schematic representation of the molecular interactions between selected pulp-derived metabolites of *Oenocarpus bataua* and α-glucosidase (PDB ID: 3A4A). Compounds: (1) Procyanidin B2; (2) Isoschaftoside; (3) Corymboside; (4) Procyanidin B1; (5) Procyanidin B3; (6) Pheophorbide A.

(A) Three-dimensional visualization of ligand binding within the catalytic domain (active site) of 3A4A. (B) Two-dimensional interaction maps illustrating hydrogen bonds, π–π stacking, π–cation interactions, and hydrophobic contacts between each ligand and key active-site residues.

General analysis

Procyanidin B2 emerged as the most potent inhibitor in the docking dataset against α-glucosidase (PDB ID: 3A4A), exhibiting a binding affinity of ΔG = −11.2 kcal/mol, which surpassed that of the reference drug acarbose (ΔG = −9.1 kcal/mol) under the same computational conditions. In the case of human pancreatic α-amylase (PDB ID: 4GQR), procyanidin B2 also demonstrated strong affinity (ΔG = −9.0 kcal/mol), yielding a mean dual-enzyme binding value of −10.1 kcal/mol.

This balanced inhibitory profile can be attributed to its multivalent interaction capacity within the catalytic domains of both enzymes. For α-amylase, procyanidin B2 forms hydrogen bonds with key catalytic residues Asp197 and Glu233, reinforced by π–anion interactions with Asp300, thereby targeting the catalytic triad responsible for substrate hydrolysis. In α-glucosidase, the ligand establishes an extensive hydrogen-bonding network involving Ser240, Ser241, Asp242, and Pro312, along with π–cation interactions with His280, contributing to stable anchoring within the active pocket.

The combination of strong catalytic residue engagement and complementary aromatic interactions underscores the structural adaptability of procyanidin B2 and supports its potential as a dual-target inhibitor capable of modulating both α-amylase and α-glucosidase activities.

This interaction profile is consistent with recent molecular docking investigations employing the same α-glucosidase structural model (PDB ID: 3A4A), which identify His280, Tyr158, and Arg315 as key anchoring residues for high-affinity inhibitors[25-28]. The involvement of these residues in π-stacking, π–cation, and hydrogen-bonding interactions underscores their central role in stabilizing ligand binding within the catalytic cavity.

The oligomeric structure of procyanidin B2 confers extended surface complementarity, enabling simultaneous engagement of multiple polar and aromatic residues. This multivalent binding capacity represents a well-established structure–activity relationship for condensed

tannins, which often display enhanced inhibitory potency due to their ability to occupy larger regions of the active site and form cooperative non-covalent interactions. Such structural features likely underpin the superior binding affinity observed for procyanidin B2 and support its potential as a dual glycosidase inhibitor.

The predicted binding affinity of procyanidin B2 ($\Delta G = -11.2$ kcal/mol) surpasses values reported for leading metabolites in recent botanical docking studies targeting the same α-glucosidase model (PDB ID: 3A4A). For instance, 4′,6,7-trimethoxyflavonol identified from Ilex guayusa exhibited a binding affinity of −8.3 kcal/mol, mediated by hydrogen bonding with Arg315 and Asp242 and hydrophobic complementarity enhanced by methoxy substituents.

Although procyanidin B2 lacks methoxy groups, its catechol-rich framework provides an alternative strategy for dual polar and hydrophobic engagement. The multiple hydroxyl groups enable extensive hydrogen bonding with catalytic and peripheral residues, while the aromatic rings support π-stacking and hydrophobic stabilization within the active pocket. This structural arrangement likely accounts for its superior predicted affinity and reinforces the importance of multivalent interaction capacity in glycosidase inhibition.

Nevertheless, as highlighted by de los Monteros-Silva et al.[29] , high *in silico* binding affinity does not necessarily translate directly into biological efficacy within complex plant extracts. Matrix effects, compound stability, solubility, and potential synergistic or antagonistic interactions can significantly influence *in vitro* and *in vivo* outcomes. Therefore, although the docking results position procyanidin B2 as a promising dual-target inhibitor, further biochemical and kinetic validation is required to substantiate its functional relevance in the context of whole-extract bioactivity.

Procyanidins are widely recognized for their multifaceted antidiabetic properties, including potent antioxidant activity and the capacity to modulate digestive enzymes. In particular, procyanidins have been shown to induce conformational changes in α-amylase, thereby reducing catalytic efficiency and limiting carbohydrate hydrolysis[30,31]. These structural perturbations are typically mediated through multivalent hydrogen bonding and hydrophobic interactions within or near the active site, which can alter substrate accessibility and enzyme dynamics.

The pronounced binding preference of procyanidin B2 toward α-glucosidase observed in the present docking analysis suggests a degree of structural optimization for this enzyme. Such selectivity may be advantageous in the development of targeted inhibitors, as preferential α-glucosidase inhibition is often associated with improved postprandial glucose control and potentially reduced gastrointestinal adverse effects compared with non-selective, broad-spectrum inhibitors such as acarbose.

Accordingly, the structural framework of procyanidin B2 may provide a valuable template for the rational design of more selective glycosidase inhibitors, aiming to balance efficacy with tolerability in antidiabetic therapeutic strategies.

Comparison with literature

The present findings are consistent with previous reports identifying oligomeric procyanidins and flavonoid glycosides as effective α-amylase and α-glucosidase inhibitors through complementary hydrogen bonding and hydrophobic interactions within catalytic pockets[32]. Such polyphenolic scaffolds are known to exploit both polar and aromatic residues, enabling multivalent binding that enhances inhibitory potency.

Notably, the predicted binding affinity of procyanidin B2 toward α-glucosidase (ΔG = −11.2 kcal/mol) substantially exceeds values reported for several recently described synthetic inhibitors. For example, Şahin et al.[33] identified triazole-ester derivatives with a maximum α-amylase affinity of −8.2 kcal/mol, while El-Sofany et al.[34] reported thiazolone hybrids reaching −7.0 kcal/mol against the same enzymatic target. Even within natural product-based investigations, Fatema et al.[32] reported a highest docking affinity of −8.0 kcal/mol for *Rorippa indica* metabolites targeting α-amylase.

Importantly, seven of the top ten *Oenocarpus bataua* metabolites identified in this study surpassed these reference benchmarks for at least one enzyme. In particular, procyanidin B2, isoschaftoside (ΔG = −11.5 kcal/mol for α-glucosidase), and corymboside (ΔG = −10.3 kcal/mol for α-glucosidase) demonstrated notably strong predicted glucosidase inhibition. These comparative results underscore the competitive binding performance of *O. bataua* metabolites and further support their potential as promising scaffolds for the development of selective glycosidase inhibitors.

The clinical relevance of dual α-amylase/α-glucosidase inhibition has gained increasing attention as a strategy to attenuate postprandial glycemic excursions while potentially improving tolerability compared with single-target agent[35]. Simultaneous modulation of both enzymes may allow a more gradual reduction in carbohydrate digestion, thereby limiting abrupt glucose spikes and reducing the likelihood of gastrointestinal side effects commonly associated with strong, non-selective inhibitors.

In this context, the observation that procyanidins consistently outperformed pulp-associated metabolites (e.g., isorhamnetin-3-glucoside, mean $\Delta G = -9.0$ kcal/mol) suggests a tissue-specific biosynthetic allocation toward structurally complex defensive compounds with antidiabetic potential. Such metabolic specialization has also been described in other Amazonian palms, where seeds frequently accumulate condensed tannins and related polyphenols with protective and bioactive functions[36].

Nevertheless, superior *in silico* binding affinity does not guarantee proportional biological efficacy. As highlighted by de los Monteros-Silva et al.[29] in the context of *Ilex guayusa* extracts targeting α-glucosidase, matrix effects, compound stability, and synergistic or antagonistic interactions among metabolites can significantly influence functional outcomes in crude preparations. Therefore, the promising docking performance of procyanidins warrants further validation through *in vitro* kinetic assays, bioavailability assessments, and fractionation studies aimed at isolating procyanidin-enriched fractions for targeted enzymatic evaluation.

Physicochemical properties and pharmaceutical similarity

Table 5 summarizes the physicochemical parameters of the ten metabolites prioritized from the molecular docking analysis of *Oenocarpus bataua*, selected based on their most negative mean ΔG values across both enzyme targets.

Molecular weight (MW) values ranged from 446.12 g/mol (Compound 9: isorhamnetin-3-glucoside) to 866.77 g/mol (Compound 10: kaempferol-3-O-robinobioside). Notably, eight compounds (C1–C7 and C10) exceeded the Lipinski molecular weight threshold (≤ 500 Da), reflecting the structurally complex and polyphenolic nature of these metabolites.

Predicted lipophilicity (MLogP) values varied between 0.53 (C9) and 3.31 (C7), indicating moderate polarity overall. Aqueous solubility (LogS) predictions classified Compounds 1, 3, 4,

612 6, 8, and 9 as soluble, whereas Compounds 2, 5, 7, and 10 were predicted to be poorly soluble,
613 which may limit their oral bioavailability[37]. Regarding drug-likeness according to Lipinski's
614 rule of five, only Compound 8 fully complied with all criteria (zero violations), highlighting
615 comparatively favorable drug-like characteristics. In contrast, Compounds 1–7 and 10 each
616 presented three rule violations, primarily due to elevated molecular weight and an excessive
617 number of hydrogen bond donors and acceptors. These properties suggest potential limitations
618 in membrane permeability and oral absorption[38]. Collectively, while several *O. bataua*
619 metabolites exhibit strong predicted enzyme-binding affinities, their physicochemical profiles
620 indicate possible challenges in pharmaceutical development. These findings underscore the
621 importance of structural optimization, delivery strategies, or semi-synthetic modification to
622 enhance drug-likeness while preserving biological activity.

Table 5 | Selected physicochemical properties of metabolites

	1	2	3	4	5	6	7	8	9	10
MW (g/mol)	562.52	578.52	564.49	578.52	578.14	594.52	866.21	453.55	446.12	866.77
Fraction Csp3	0.2	0.2	0.42	0.2	0.2	0.44	0.2	0.95	0.318	0.2
n-ROTB	3	3	4	3	3	6	5	23	4	5
n-ON acceptors	11	12	14	12	12	15	18	8	10	18
n-OHNH donors	9	10	10	10	10	9	15	3	6	15
MR	145.64	146.71	133.26	146.71	146.71	139.36	219.09	120.21	111.08	219.09
TPSA (Å2)	200.53	220.76	250.97	220.76	220.76	249.2	331.14	138.12	170.05	331.14
MLogP	3.27	-0.26	-3.97	2.37	2.37	-3.43	3.31	1.91	0.53	-1.11
WS Log S (Ali)	M.Sol	P.Sol	Sol	M.Sol	P.Sol	M.Sol	P.Sol	M.Sol	Sol	P.Sol
DLLR	3	3	3	3	3	3	3	0	1	3
BS	0.17	0.17	0.17	0.17	0.17	0.17	0.17	0.55	0.55	0.17
Leadlikeness	1	1	1	1	1	1	1	2	1	1

Notes. MW: Molecular Weight, Csp3: Fraction of carbon atoms in the sp3 hybridization, n-ROTB: Number of Rotatable Bonds, n-ON acceptors: Number of hydrogen bond acceptors, n-OHNH donors: Number of hydrogen bonds donors, MR: Molecular refractivity, TPSA: Topological Polar Surface Area, MLogP: logarithm of partition coefficient of compound between n-octanol and water, WS: Water solubility, DLLR: Number of violations of Drug likeness Lipinski rule, BS: Bioavailability Score, Lead likeness violation violations (MW > 500, log P > 5). Sol: soluble, P.Sol: Poorly soluble, M.Sol: Moderately soluble.

Compounds. 1: Procyanidin B2, 2: Isoschaftoside, 3: Corymboside, 4: Procyanidin B1, 5: Procyanidin B3, 6: Pheophorbide A. 7: Procyanidin C1. 8: 3-Genistein-8-C-glucoside, 9: Isorhamnetin-3-glucoside, 10: Kaempferol-3-O-robinobioside

Pharmacokinetic profile (ADME)

Predicted intestinal absorption differed substantially among the evaluated metabolites. Among the ten prioritized compounds, only procyanidin C1 (C7) was predicted to exhibit high gastrointestinal absorption (GIA), suggesting comparatively favorable oral uptake. All remaining compounds—including procyanidins B1–B3 (C1, C4, C5), isoschaftoside (C2), corymboside (C3), pheophorbide A (C6), 3-genistein-8-C-glucoside (C8), isorhamnetin-3-glucoside (C9), and kaempferol-3-O-robinobioside (C10)—were predicted to have low GIA. This trend is consistent with their relatively high polarity, multiple hydroxyl groups, and glycosylated frameworks, which limit passive diffusion across the intestinal epithelium.

Caco-2 permeability predictions further supported these observations. All compounds exhibited very low apparent permeability (log Papp values ranging from −6.68 to −5.48), indicating restricted transcellular transport and reinforcing the expectation of limited oral bioavailability for most structures. In addition, predicted skin permeability was uniformly low (log Kp between −7.39 and −11.3 cm/s), effectively excluding transdermal administration as a feasible delivery route.

Overall, although several *O. bataua* metabolites demonstrated strong predicted enzyme-binding affinities, their pharmacokinetic profiles suggest limited systemic absorption following oral administration. These findings highlight the potential need for formulation strategies, targeted delivery systems, or structural optimization to enhance bioavailability while preserving biological activity.

Predicted interactions with membrane transporters revealed heterogeneous ADME behavior among the evaluated metabolites. Several compounds—including isoschaftoside (C2), corymboside (C3), procyanidins B1 and B3 (C4 and C5), pheophorbide A (C6), and kaempferol-3-O-robinobioside (C10)—were identified as potential substrates of P-glycoprotein (P-gp). This efflux transporter plays a central role in limiting intracellular accumulation and intestinal absorption; therefore, P-gp substrate status may further reduce systemic exposure of these molecules. Conversely, isoschaftoside (C2), procyanidin B1 (C4), and kaempferol-3-O-robinobioside (C10) were also predicted to act as P-gp inhibitors. This dual substrate–inhibitor profile suggests a potential risk of transporter-mediated drug–drug interactions, particularly if administered in combination with other P-gp substrates. Such interactions could alter pharmacokinetics by modifying efflux dynamics at intestinal, hepatic, or blood–brain barrier interfaces.

Regarding tissue distribution, only 3-genistein-8-C-glucoside (C8) was predicted to penetrate the blood–brain barrier (BBB), indicating a theoretical capacity for central nervous system exposure. All other compounds were classified as non-penetrant, suggesting that their distribution would likely remain peripheral. From a therapeutic perspective targeting postprandial glycemic control, limited BBB penetration may be advantageous by minimizing potential central nervous system-related adverse effects.

Predicted steady-state volume of distribution (VDss) values suggested overall moderate tissue partitioning among the evaluated metabolites. Procyanidin B3 (C5) exhibited the highest predicted VDss, indicating comparatively greater distribution into peripheral tissues relative to the other compounds. In contrast, procyanidin B2 (C1) and procyanidin C1 (C7) showed lower VDss values, implying a tendency toward confinement within plasma and extracellular compartments. Such distribution characteristics may influence both therapeutic efficacy and elimination kinetics.

Plasma protein binding predictions further indicated variability in the fraction of unbound (free) drug. Procyanidin B3 (C5) and 3-genistein-8-C-glucoside (C8) demonstrated relatively higher predicted free fractions, potentially enhancing their pharmacologically active concentrations. Conversely, procyanidin B2 (C1) was predicted to exhibit near-complete protein binding, which may restrict its effective systemic exposure despite its strong *in silico* binding affinity to enzymatic targets.

Taking together, these distribution and binding profiles underscore the complexity of translating docking affinity into pharmacodynamic relevance, as tissue partitioning and protein association can substantially modulate the bioactive fraction available for enzyme inhibition *in vivo*.

Predicted metabolic liability indicated generally limited involvement of major cytochrome P450 (CYP) isoforms for most compounds. Procyanidin B3 (C5) was the only metabolite predicted to act as a CYP3A4 substrate, suggesting potential susceptibility to hepatic first-pass metabolism. Notably, this compound was also predicted to inhibit CYP2D6, CYP2C9, and CYP1A2, indicating a comparatively higher risk of metabolic drug–drug interactions. Procyanidin B2 (C1) was predicted to inhibit CYP2C9 and CYP1A2, whereas the remaining metabolites demonstrated minimal inhibitory activity toward principal CYP isoforms, suggesting a lower probability of CYP-mediated interaction liabilities.

Transporter-mediated hepatic disposition may also contribute to elimination pathways for selected structures. Procyanidin B3 (C5) showed predicted interactions with organic anion transporting polypeptides OATP1B1 and OATP1B3, while kaempferol-3-O-robinobioside (C10) demonstrated predicted affinity for breast cancer resistance protein (BCRP) and OATP1B3. These transporter associations may influence hepatic uptake, biliary excretion, and systemic clearance.

Renal clearance predictions revealed variability in elimination kinetics. Kaempferol-3-O-robinobioside (C10) exhibited the highest predicted renal clearance, consistent with efficient excretory elimination. In contrast, procyanidin C1 (C7) displayed comparatively low predicted clearance, suggesting potential systemic persistence. Estimated half-life values were generally short, indicating rapid elimination for most compounds. However, isoschaftoside (C2), procyanidin B1 (C4), and kaempferol-3-O-robinobioside (C10) demonstrated relatively longer predicted half-lives, which may prolong systemic exposure and potentially enhance pharmacodynamic effects.

Collectively, these ADME predictions suggest that while several *O. bataua* metabolites display strong enzyme-binding affinities, their pharmacokinetic profiles vary considerably and may influence their translational potential as orally active antidiabetic agents.

Toxicological profile

In silico toxicity predictions indicated a heterogeneous safety profile among the prioritized metabolites. Mutagenicity alerts were identified for corymboside (C3) and isorhamnetin-3-glucoside (C9), suggesting a potential genotoxic risk that warrants experimental verification through *in vitro* and *in vivo* assays. Importantly, all evaluated compounds were predicted to be non-carcinogenic.

Drug-induced liver injury (DILI) liability was predicted for procyanidin B2 (C1), isoschaftoside (C2), procyanidin B1 (C4), and kaempferol-3-O-robinobioside (C10), indicating that hepatic safety assessment and monitoring would be essential during further development. Ocular irritation alerts were observed for Compounds 1, 2, 4, and 7, whereas none of the metabolites were predicted to induce skin sensitization.

Ecotoxicological predictions also revealed variable environmental risk. Most compounds were predicted to be toxic to *Daphnia magna*, with the exception of procyanidin C1 (C7) and 3-genistein-8-C-glucoside (C8). All compounds were predicted to be non-toxic to *Tetrahymena pyriformis*. In addition, potential bee toxicity was indicated for isoschaftoside (C2), procyanidin B1 (C4), pheophorbide A (C6), procyanidin C1 (C7), and kaempferol-3-O-robinobioside (C10).

Overall, while the predicted toxicological profiles do not indicate overt carcinogenic liability, certain metabolites exhibit mutagenicity or hepatotoxicity alerts that necessitate comprehensive experimental validation. These findings emphasize the importance of early-stage toxicological screening when considering phenolic-rich natural products for pharmaceutical development.

Therapeutic Implications

From a pharmacokinetic standpoint, procyanidin C1 (C7) emerges as the most promising oral candidate among the evaluated metabolites. Its predicted high gastrointestinal absorption, moderate tissue distribution, and comparatively favorable metabolic interaction profile support its potential for systemic exposure following oral administration. 3-Genistein-8-C-glucoside (C8) is distinguished by its predicted blood–brain barrier permeability and relatively low toxicity alerts, suggesting possible relevance for neurological or neuro-metabolic applications (**Table 6**). Although central nervous system exposure is not essential for glycemic control, this property may broaden its therapeutic scope, particularly in the context of diabetes-associated neurodegenerative complications.

In contrast, despite favorable distribution characteristics, procyanidin B3 (C5) presents a higher likelihood of metabolic drug–drug interactions due to predicted CYP inhibition and transporter involvement, which may complicate clinical translation. Glycosylated flavonoids with poor gastrointestinal absorption and predicted P-gp efflux liability would likely require advanced formulation strategies (e.g., nanoencapsulation or delivery systems enhancing permeability) to achieve therapeutically relevant concentrations.

Compounds C3 (corymboside) and C9 (isorhamnetin-3-glucoside) require caution due to predicted mutagenicity alerts, while metabolites flagged for potential drug-induced liver injury (DILI) necessitate dedicated hepatic safety assessment in subsequent preclinical studies.

Overall, Compounds C7 and C8 exhibit the most balanced combination of predicted pharmacokinetic properties and safety parameters, positioning them as priority candidates for further experimental validation and lead optimization.

Table 6 | Summary of predicted pharmacokinetic (ADME) and toxicity properties of the prioritized metabolites identified from *Oenocarpus bataua* extracts

Compound	1	2	3	4	5	6	7	8	9	10
Absorption										
Caco2 (log Papp in 10^{-6} cm/s)	-6.32	-6.62	-6.46	-6.62	-5.68	-6.68	-5.52	-5.48	-6.44	-6.18
GIA	Low	Low	Low	Low	Low	Low	High	Low	Low	Low
Skin Permeability log Kp (cm/s)	-7.4	-8.15	-11.3	-8.15	-7.96	-9.91	-8.58	-7.39	-11.3	-9.24
P-Glycoprotein Inhibitor	No	Yes	No	Yes	No	No	No	No	No	Yes
P-Glycoprotein Substrate	No	Yes	Yes	Yes	Yes	Yes	No	No	No	Yes
Distribution										
BBB	N. P	N. P	N. P	N. P	N. P	N. P	N. P	P	N. P	N. P
Fraction Unbound (Human)	0.72	0.81	0.65	0.81	1.4	0.83	0.43	1.04	0.65	0.68
PPB (%)	100.2	80.58	68.5	80.2	87.75	71.75	22.69	50.28	-9.39	71.23
Vdss	0.08	0.46	0.87	0.46	1.95	0.78	0.26	0.55	0.87	0.46
Metabolism										
CYP 3A4 Substrate	No	No	No	No	Yes	No	No	No	No	No
CYP 3A4 Inhibitor	No	No	No	No	No	No	No	No	No	No
CYP 2D6 Inhibitor	No	No	No	No	Yes	No	No	No	No	No
CYP 2C9 Inhibitor	Yes	No	No	No	Yes	No	No	No	No	No
CYP 1A2 Inhibitor	Yes	No	No	No	Yes	No	No	No	No	No
BCRP	No	No	No	No	No	No	No	No	No	Yes
OATP1B1	No	No	No	No	Yes	No	No	No	No	No
OATP1B3	No	No	No	No	Yes	No	No	No	No	Yes
Excretion										
Total renal clearance (log mL/min/kg)	0.104	0.319	0.19	0.321	0.548	0.173	0.035	0.115	0.186	0.63
OCT 2	10.99	11.84	8.38	11.85	5.42	11.91	1.57	3.92	8.28	10.39
Half-Life of Drug	0.49	0.907	0.003	0.907	0.158	0.026	0.002	0.02	0.003	0.99
Toxicity										
AMES Mutagenesis	Safe	Safe	Toxic	Safe	Safe	Safe	Safe	Safe	Toxic	Safe
Carcinogenicity	Safe	Safe	Safe	Safe	Safe	Safe	Safe	Safe	Safe	Safe
DILI	Toxic	Toxic	Safe	Toxic	Safe	Safe	Safe	Safe	Safe	Toxic

Skin Sensitisation	No	No	No	No	No	No	No	No	No	No
Eyes irritation	Toxic	Toxic	Safe	Toxic	Safe	Safe	Toxic	Safe	Safe	Safe
Daphnia Magna	Toxic	Toxic	Toxic	Toxic	Toxic	Toxic	Safe	Safe	Toxic	Toxic
Tetrahymena Pyriformis	Safe	Safe	Safe	Safe	Safe	Safe	Safe	Safe	Safe	Safe
Bee toxicity	Safe	Toxic	Safe	Toxic	Safe	Toxic	Toxic	Safe	Safe	Toxic

Notes. Caco-2: Colon adenocarcinoma permeability. GIA: Gastrointestinal absorption. BBB: Blood–Brain Barrier permeability (N.P: Non-Penetrable, P: Penetrable), PPB: Plasma Protein Binding (%), VDss: Steady-state volume of distribution, CYP: Cytochrome P450, BCRP: Breast Cancer Resistance Protein, OATP: Organic anion transporting polypeptides, OCT2: Organic cation transporter 2. DILI: Drug-Induced Liver Injury.

Compounds. 1: Procyanidin B2, 2: Isoschaftoside, 3: Corymboside, 4: Procyanidin B1, 5: Procyanidin B3, 6: Pheophorbide A. 7: Procyanidin C1. 8: 3-Genistein-8-C-glucoside, 9: Isorhamnetin-3-glucoside, 10: Kaempferol-3-O-robinobioside

Pathway analysis

A total of 17 metabolites were successfully mapped to metabolic pathways using the Kyoto Encyclopedia of Genes and Genomes (KEGG) database, including 16 compounds annotated at confidence level 2 and one at level 3 (**Table S8**). The majority of these metabolites were associated with the phenylpropanoid biosynthesis pathway, which integrates interconnected metabolic routes such as flavonoid biosynthesis, the shikimate pathway, and primary carbon metabolism, including the citrate (TCA) cycle. Within the phenylpropanoid biosynthesis network, several central intermediates were identified, including phenylalanine, tyrosine, shikimic acid, chlorogenic acid, salicylic acid, epicatechin, naringenin, and citric acid (**Fig. 6**). These metabolites represent key nodes linking primary metabolism with the production of structurally diverse phenolic compounds. More specifically, apigenin, naringenin, and epicatechin were mapped to the flavonoid biosynthesis pathway, highlighting active flavonoid diversification. Chlorogenic acid and salicylic acid were directly assigned to hydroxycinnamate metabolism within the broader phenylpropanoid pathway. Shikimic acid, phenylalanine, and tyrosine were linked to the shikimate pathway and its downstream phenylpropanoid derivatives, emphasizing the role of aromatic amino acid metabolism in driving secondary metabolite biosynthesis.

In addition, citric acid was mapped to the citrate cycle (TCA cycle), reflecting the integration of energy metabolism with specialized metabolite production. Collectively, these pathway

assignments underscore the metabolic connectivity between primary carbon flux and phenolic biosynthesis in *Oenocarpus bataua*, supporting the biochemical basis for the antioxidant and enzyme-inhibitory activities observed experimentally.

Metabolites exhibiting significant differences among fruit tissues (**Figs. 2C** and **2D**) were predominantly associated with central metabolic pathways, particularly phenylpropanoid biosynthesis derived from the shikimate pathway. This distribution pattern was further corroborated by individual sample analysis in the heatmap, where phenylalanine and shikimic acid displayed higher relative abundances in pulp samples. Such enrichment suggests enhanced metabolic flux through the shikimate–phenylpropanoid axis in the pulp tissue.

These intermediates are not only precursors of flavonoids and other phenolic compounds but also play important roles in determining fruit sensory attributes. Sugars and organic acids contribute directly to sweet and sour taste perception, while fatty acids and amino acids act as precursors of volatile compounds that define fruit aroma and overall quality[39]. The elevated levels of shikimate-derived metabolites in the pulp therefore reflect both active secondary metabolism and biochemical processes linked to fruit ripening, flavor development, and ecological interactions with seed dispersers.

In peel tissues, higher relative abundances of tyrosine, chlorogenic acid, apigenin, and citric acid were detected, reflecting the involvement of multiple interconnected pathways, including the shikimate pathway, hydroxycinnamate metabolism (phenylpropanoid biosynthesis), flavonoid biosynthesis, and the citrate (TCA) cycle. Among these metabolites, chlorogenic acid represents a major phenolic constituent with well-documented roles in plant defense against abiotic stress and significant contribution to antioxidant capacity. Its accumulation has been associated with modulation of ethylene production and mitigation of postharvest deterioration processes, including softening, browning, firmness loss, and oxidative damage[39,40]. These findings are consistent with the protective and barrier-related function of the peel as the outermost tissue exposed to environmental stressors.

In seed samples, salicylic acid, epicatechin, and naringenin were identified and mapped to hydroxycinnamate metabolism and flavonoid biosynthesis pathways. Flavonoids in seeds are

widely recognized for their roles in scavenging reactive oxygen species and functioning as signaling molecules involved in the regulation of dormancy and germination processes[41]. The enrichment of these metabolites in seed tissue underscores their physiological importance in safeguarding embryonic integrity and coordinating stress-responsive and developmental signaling pathways.

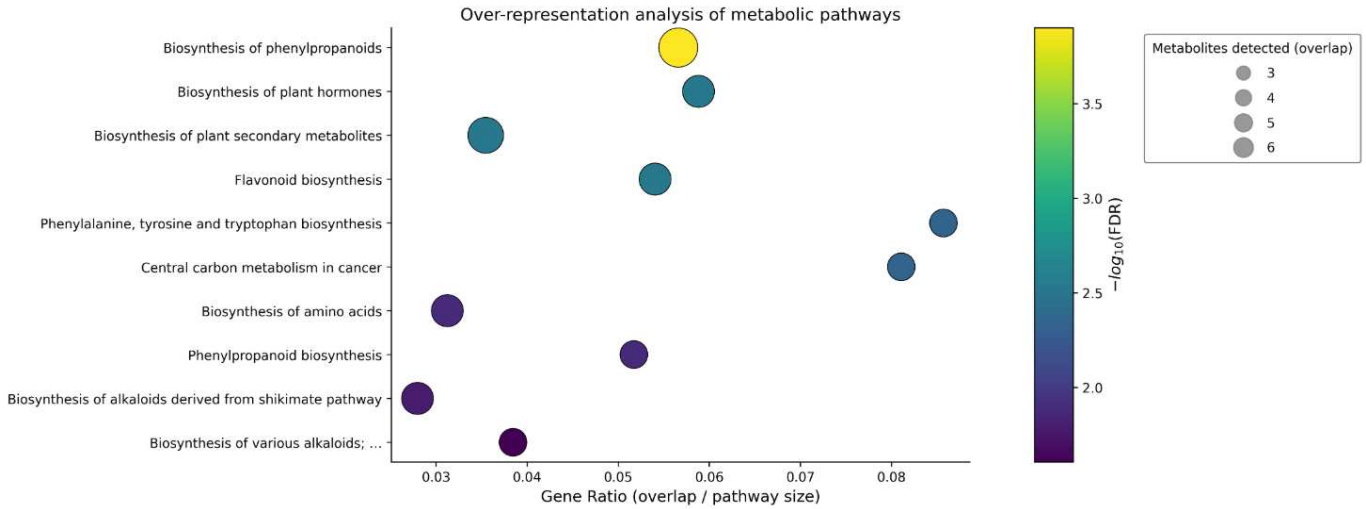

Fig. 6 | KEGG pathway overrepresentation analysis of metabolites identified in *Oenocarpus bataua* extracts. The y-axis lists the enriched metabolic pathways, while the x-axis represents the ratio of detected metabolites mapped to each pathway relative to the total number of annotated metabolites. Dot size reflects the number of metabolites associated with each pathway, and color intensity indicates statistical significance expressed as $-\log_{10}$ (FDR), ranging from yellow (highly significant enrichment) to purple (lower significance).

The most prominently enriched pathways include phenylpropanoid biosynthesis, plant hormone biosynthesis, flavonoid biosynthesis, and the broader biosynthesis of plant secondary metabolites, underscoring the coordinated metabolic investment in phenolic and signaling compounds that contribute to the biological activities observed in *O. bataua* tissues.

Hydroethanolic extracts of *Oenocarpus bataua* Mart. demonstrated pronounced tissue-specific bioactivity profiles. Seed extracts exhibited the highest total phenolic content and the strongest

antioxidant capacity across DPPH, ABTS, and FRAP assays, consistent with their enrichment in procyanidins, flavan-3-ols, and stilbene-related metabolites.

Both seed and pulp extracts displayed potent α-amylase inhibitory activity, surpassing the reference drug acarbose under the experimental conditions employed. In contrast, α-glucosidase inhibition followed a distinct distribution pattern, with pulp and peel extracts showing greater activity than seed, underscoring enzyme-specific differences in metabolite interactions.

UPLC–ESI–QTOF–MS/MS profiling enabled the annotation of a chemically diverse array of specialized metabolites, including procyanidins and flavonols (e.g., tricin/tricetin- and isorhamnetin-related derivatives). Molecular docking analyses further supported the capacity of procyanidin-class compounds to establish stable interactions within the catalytic domains of human pancreatic α-amylase and α-glucosidase, providing mechanistic insight into the experimentally observed enzyme modulation.

Collectively, these results identify *O. bataua* as a metabolite-rich Amazonian species exhibiting combined antioxidant properties and inhibitory activity against key carbohydrate-hydrolyzing enzymes. The findings support its potential as a source of bioactive scaffolds for glycemic control. Future studies should focus on *in vivo* validation, bioavailability and metabolic profiling, and the isolation or standardization of compounds most strongly associated with α-amylase and α-glucosidase inhibition.

Methods

Fruit collection and sample preparation

Fresh fruits of *Oenocarpus bataua* Mart. were obtained from a local market in Parroquia Puerto Napo, Tena, Napo Province, Ecuador (1°02′19.2″S, 77°45′41.8″W). Upon arrival at the laboratory, fruits were manually separated into peel, pulp, and seed fractions. Each fraction was freeze-dried using a lyophilizer (SP Scientific–Genevac BTP-9E LOVE) for a minimum of 72 h to ensure complete moisture removal. The dried materials were subsequently ground to a fine powder using a laboratory mill and stored at −20 °C until extraction. For extraction, 1.0 g of powdered material from each fraction was mixed with 10 mL of a 70:30 (v/v) ethanol–water solution. The mixtures were subjected to ultrasonic-assisted extraction for 30 min, followed by centrifugation at 4000 rpm for 15 min. The resulting supernatants were transferred into 5 mL amber vials and stored at −4 °C

prior to analysis. Extraction yields differed among fruit tissues, with the seed fraction exhibiting the highest extractive yield (6.30%), followed by pulp (5.80%) and peel (3.70%), indicating tissue-dependent differences in extractable metabolite content.

Total phenolic, flavonoid content and antioxidant capacity

The antioxidant activity of *Oenocarpus bataua* Mart. extracts was assessed using three complementary *in vitro* assays: DPPH (2,2-diphenyl-1-picrylhydrazyl), ABTS (2,2′-azino-bis(3-ethylbenzothiazoline-6-sulfonic acid)) and FRAP (Ferric Reducing Antioxidant Power). While DPPH and ABTS assays evaluate the free radical scavenging capacity of the extracts, the FRAP assay measures their reducing power by quantifying the ability to convert Fe^{3+} to Fe^{2+}. Together, these methods offer a comprehensive evaluation of antioxidant potential. To further characterize the bioactive profile, total phenolic and flavonoid contents were quantified, providing insight into the compounds likely responsible for the observed antioxidant activity.

Total Phenol Content

The total phenolic content of each extract was determined using the Folin–Ciocalteu colorimetric assay (Supelco®), with gallic acid employed as the calibration standard. A working solution of each extract (1 mg/mL, prepared by dissolving 5 mg of dried sample in 5 mL of ethanol) was mixed with 860 µL of distilled water and 40 µL of Folin–Ciocalteu reagent under light-protected conditions. After a 5-minute incubation at room temperature, 100 µL of a 7% (w/v) sodium carbonate solution was added. The reaction mixture was then incubated for 60 minutes at room temperature. Absorbance was measured at 750 nm using a UV-Vis spectrophotometer (Shimadzu UV-1280). Quantification was performed using a gallic acid calibration curve (25–500 µg/mL), and results were expressed as micrograms of gallic acid equivalents (µg GAE) per milligram of extract[42].

Total flavonoid content

Total flavonoid content was quantified using a modified aluminum chloride ($AlCl_3$) colorimetric assay, with quercetin as the calibration standard[43]. Freeze-dried aqueous extracts were reconstituted

in distilled water at the same concentration used for total phenolic analysis. An aliquot of 1 mL of the diluted extract was mixed with 1 mL of a 2% (w/v) $AlCl_3$ solution and incubated at room temperature for 10 minutes. The absorbance of the resulting complex was measured at 438 nm using a UV-Vis spectrophotometer (Shimadzu UV-1280). Quantification was performed using a standard curve constructed with quercetin (1–16 µg/mL), and results were expressed as micrograms of quercetin equivalents (µg QE) per milligram of freeze-dried extract.

DPPH free radical scavenging activity

The DPPH (2,2-diphenyl-1-picrylhydrazyl) radical scavenging activity was assessed using 96-well microplates. In each well, 100 µL of ethanolic extract at varying concentrations was combined with 100 µL of 96% ethanol. Subsequently, 50 µL of a freshly prepared DPPH solution (0.06 mM in 96% ethanol) was added. The reaction mixtures were incubated in the dark at room temperature for 30 min with constant agitation (60 rpm) using an orbital shaker (Orbit™ LS Low Speed Laboratory Shaker, Labnet, Edison, NJ, USA)[44].

Absorbance was measured at 517 nm using a GloMax® microplate reader (Promega Corporation, Madison, WI, USA). All measurements were performed in triplicate. Trolox was used as the reference antioxidant, and a standard curve was constructed for quantification. The antioxidant capacity of the samples was expressed as Trolox Equivalent Antioxidant Capacity (TEAC, mg TE/g extract). Each assay was independently repeated three times.

The radical scavenging activity (RSA) was calculated using the following equation:

$$\mathrm{DPPH_{RSA}}\ (\%) = \frac{(\mathrm{Abs_{control}} - \mathrm{Abs_{sample}}) * 100}{\mathrm{Abs\ control}} \qquad (1)$$

where $Abs_{control}$ refers to the absorbance of the DPPH solution with ethanol (solvent), and Abs_{sample} is the absorbance of the DPPH solution in the presence of the extract or standard.

The half-maximal inhibitory concentration (IC_{50}) was determined by fitting the inhibition data to a sigmoidal dose-response model (Equation 2), using nonlinear regression:

$$Y = \frac{100}{(1+10^{((\mathrm{LogIC_{50}}-X)*\ \mathrm{HillSlope})})} \quad (2)$$

Finally, the antioxidant activity was expressed as Trolox Equivalent Antioxidant Capacity (TEAC), calculated using the following relationship (Equation 3)[45].

$$\mathrm{TEAC} = \frac{\mathrm{IC_{50}\,of\ Trolox}\left(\frac{\mu g}{L}\right)}{\mathrm{IC_{50}\,of\ sample}\left(\frac{\mu g}{L}\right)} \quad (3)$$

ABTS free radical scavenging activity

The ABTS assay was conducted following a modified version of the method described by Re *et al.*,[46]. The $ABTS^{+}$ stock solution was prepared by mixing 7 mM ABTS with 2.45 mM potassium persulfate in distilled water and allowing the mixture to react in the dark for 16 h at room temperature. The resulting radical cation solution was diluted with ethanol to an absorbance of 0.70 ± 0.02 at 734 nm, measured using a UV-Vis spectrophotometer (Shimadzu 3600 Plus, Kyoto, Japan).

Samples were dissolved in ethanol and sonicated for 5 min. For the assay, 150 µL of extract or Trolox standard was added to 2850 µL of $ABTS^{+}$ solution. After 6 min of incubation at room temperature, absorbance was read at 734 nm. A calibration curve with Trolox (1–20 µg/mL) was used, and results were expressed as mg Trolox equivalents per gram of dry weight (mg TE/g dw). All measurements were done in triplicate.

The RSA was calculated using (Equation 4):

$$\mathrm{ABTS_{RSA}}\ (\%) = \left(\frac{\mathrm{Abs_{control}} - \mathrm{Abs_{sample}}}{\mathrm{Abs_{control}}}\right) * 100 \quad (4)$$

FRAP ferric reducing antioxidant power assay

The ferric reducing antioxidant power (FRAP) of the hydroethanolic extracts was determined following the method of Benzie and Strain [47], with slight modifications. The working reagent was freshly prepared by mixing acetate buffer (300 mM, pH 3.6), 10 mM TPTZ solution in 40 mM HCl, and 20 mM $FeCl_3 \cdot 6H_2O$ in a 10:1:1 (v/v/v) ratio.

For the assay, 300 µL of FRAP reagent was mixed with 30 µL of distilled water and 10 µL of extract or standard in a 96-well microplate. The mixture was incubated at 37 °C for 4 min in the dark, and the absorbance was measured at 600 nm using a Promega GloMax® Discover System microplate reader.

A calibration curve was constructed using $FeSO_4 \cdot 7H_2O$ (0–1000 µM), and results were expressed as micromoles of ferrous equivalents per gram of dry weight (µmol Fe^{2+}/g dw). All measurements were performed in triplicate.

The antioxidant capacity was calculated using Equation 5:

$$\text{FRAP}\left(\frac{\mu\text{mol Fe}^{2+}}{\text{gdw}}\right) = \frac{\text{Abs}_{\text{sample}} - \text{Abs}_{\text{blank}}}{\text{Slope of Fe}^{2+}\text{ standard curve}} \quad (5)$$

α-amylase inhibitory activity assay

The α-amylase inhibitory activity of the extracts was determined using a colorimetric method based on the 3,5-dinitrosalicylic acid (DNS) assay, following established protocols with minor modifications[48]. Briefly, 200 µL of each extract at various concentrations was mixed with 200 µL of porcine pancreatic α-amylase solution (2 U/mL) prepared in phosphate buffer (Na_2HPO_4/KH_2PO_4, 0.02 M, pH 6.9, containing 0.006 M NaCl). The mixture was incubated at room temperature for 10 min. Subsequently, 200 µL of a 1% (w/v) soluble starch solution was added, and the reaction was allowed to proceed for 5 min under the same conditions. To terminate the enzymatic reaction, 200 µL of DNS reagent (1% 3,5-dinitrosalicylic acid, 30% sodium potassium tartrate tetrahydrate, and 2 N NaOH) were added to each tube. Samples were then heated in a boiling water bath (90 °C) for 10 min and cooled to room temperature. After dilution with 5 mL of distilled water, absorbance was measured at 540 nm using a UV–VIS spectrophotometer (Shimadzu UV-3600 Plus).

Acarbose (1.6–490 µg/mL) served as the positive control. A buffer-only control and sample blanks (without enzyme) were included to correct background absorbance. The percentage of α-amylase inhibition (%αAI) was calculated using Equation 6:

$$\% \propto \mathrm{AI} = \left(\frac{B_1 - B_2}{B_1}\right) * 100 \quad (6)$$

where B_1 is the absorbance of the control reaction (with enzyme and without inhibitor) minus the control blank (no enzyme), and B_2 is the absorbance of the sample reaction minus its corresponding blank. All assays were performed in triplicate. Results were expressed as percentage inhibition and IC_{50} values (µg/mL), determined by non-linear regression analysis of log-transformed concentration–response data. Statistical differences between treatments were analyzed using one-way ANOVA, followed by Tukey's post hoc test, with $p < 0.05$ considered statistically significant.

α-glucosidase inhibitory activity assay

The inhibitory activity of the plant extracts against α-glucosidase was assessed following the procedure described by Pistia-Brueggeman and Hollingsworth [49], with minor modifications introduced to adapt the protocol. Twenty microliters (20 µL) of the extracts obtained from each fruit part at different concentrations were incubated with 10 µL of α-glucosidase enzyme solution derived from *Saccharomyces cerevisiae* (Sigma-Aldrich) at a concentration of 0.2 U/mL for 10 minutes at 37 °C, in the presence of an additional 50 µL of 0.02 M phosphate buffer (pH 6.8). After the initial 10-minute incubation, the reaction was initiated by adding 20 µL of 0.75 mM pNPG (substrate), and the mixture was further incubated for 30 minutes. The reaction was terminated by the addition of 100 µL of 0.02 M Na_2CO_3, and the final absorbance was measured at 405 nm using a GloMax® Discover microplate reader.

Acarbose was used as a positive control at varying concentrations (10–200 µg/mL). Enzyme activity was calculated in the same manner as in the α-amylase assay, according to Equation 6. Similarly, the results were expressed as percentage inhibition and IC_{50} values (µg/mL), calculated through non-linear regression analysis of log-transformed concentration–response curves. Statistical differences among treatments were evaluated using one-way ANOVA followed by Tukey's post hoc test, with $p < 0.05$ considered statistically significant.

Metabolomic profile using UPLC-MS/MS

The metabolomic profiling of the 70% hydroethanolic extracts obtained from the peel, pulp, and seed of *Oenocarpus bataua Mart.* was carried out using reversed-phase ultra-high-performance liquid chromatography (UPLC) coupled with electrospray ionization mass spectrometry (ESI–MS). Chromatographic separation was performed on a Waters Acquity UPLC BEH C18 column (2.1 × 50 mm, 1.7 µm particle size; Waters, Milford, MA, USA).

Lyophilized extracts (5 mg) were reconstituted in 1 mL of a 1:1 (v/v) water–ethanol solution, vortex-mixed, and centrifuged at 10,000 rpm for 3 min. The resulting supernatants were subjected to MS analysis. To ensure system stability and analytical reproducibility, a pooled quality control (QC) sample was prepared by combining equal aliquots of each extract and injected periodically throughout the analytical sequence. Solvent and procedural blanks were included to monitor potential background contamination[50]. The injection volume was 3 µL.

The chromatographic gradient employed a binary mobile phase consisting of (A) 0.1% formic acid in water and (B) 0.1% formic acid in acetonitrile, delivered at a flow rate of 0.2 mL/min. The gradient program was as follows: 0–1 min, 1% B; 1–10 min, 1–20% B; 10–20 min, 20–25% B; 20–25 min, 25–35% B; 25–30 min, 35–50% B; and 30–34 min, re-equilibration at 1% B.

Mass spectrometric data were acquired in both negative and positive ionization modes over an m/z range of 100–1200 Da. Source parameters for full-scan and data-dependent acquisition (DDA) analyses were set as follows: capillary voltage, 0.5 kV; sample cone voltage, 40 V; source offset, 80 V; source temperature, 120 °C; desolvation temperature, 450 °C; desolvation gas (nitrogen) flow, 900 L/h; and cone gas flow, 0 L/h. Argon was used as the collision gas. MS^1 and MS^2 spectra were acquired in resolution mode using collision energies of 10 and 20 eV.

Mass calibration was achieved via LockSpray™ using continuous infusion of leucine-enkephalin (1 ng/µL) at a flow rate of 10 µL/min. The MS^1 scan time was set to 0.2 s and the MS^2 scan time to 0.1 s, with the five most intense precursor ions automatically selected for fragmentation by collision-induced dissociation (CID). Data acquisition and processing were performed using MassLynx V4.1 software (Waters, Milford, MA, USA). The acquisition ranges were m/z 100–1200 for MS^1 and m/z 50–1200 for MS^2 in DDA mode.

Compound identification was achieved by comparing retention times and mass spectral data with those of authentic reference standards, in accordance with Level 1 identification criteria established by the Metabolomics Standards Initiative (MSI).

Data processing and annotation workflow for metabolomic profiling of *Oenocarpus bataua* Mart. Extracts

Non-targeted metabolomic data generated from data-dependent acquisition (DDA) experiments were processed using MZmine version 4.3.0 (MZmine 4 Documentation). The initial preprocessing workflow comprised noise filtering, with a minimum MS^1 peak intensity threshold of 600 (amplitude) and an MS/MS signal threshold of 40 (amplitude). To minimize interference from non-biological signals, all features detected in blank samples were removed prior to downstream analyses. A comprehensive list of data processing parameters applied to full-scan (MS^1) feature detection and alignment is provided in **raw primary data** (**Tables S1-S2**), whereas detailed MS/MS (DDA) processing settings and spectral handling parameters are available in **Tables S3.1–S4.2**.

For metabolite annotation in the absence of authentic reference standards, MS/MS spectra were submitted to the Global Natural Products Social Molecular Networking platform (GNPS2; ccms-ucsd.github.io). Raw datasets acquired on the Waters platform were converted to .mgf or .mzML formats according to standard conversion procedures. The complete dataset was deposited in the GNPS/MassIVE repository under accession number MSV000098809. All molecular networking job URLs and feature-level annotation details are included in **raw primary data Tables S5**.

Molecular network construction was performed using a precursor and fragment ion mass tolerance of 0.5 Da. Edges between nodes were retained only when supported by at least three shared fragment ions and a cosine similarity score > 0.70. The resulting feature table was subsequently filtered to include only signals with a mass accuracy within ±10 ppm and a cosine similarity score ≥ 0.70. Features meeting these criteria were classified as Level 2 identifications according to the Metabolomics Standards Initiative (MSI), corresponding to putatively annotated compounds based

on high spectral similarity to reference MS/MS libraries but lacking confirmation with authentic standards under identical experimental conditions[51].

Features that did not satisfy these thresholds were assigned Level 3 status, indicating tentative annotation at the level of compound classes inferred from spectral similarity to known chemical families reported in public databases.

The processed feature table exported from MZmine in .txt format was further curated using the notame R package to perform normalization and correct signal drift. The finalized dataset was subsequently uploaded to MetaboAnalyst 6.0 for comprehensive statistical evaluation and multivariate analysis. All analysis scripts and processed data files have been made publicly available in the GitHub repository (IKIAM-NPLab/*Oenocarpus-bataua*-Mart) to ensure transparency and reproducibility.

Pearson Correlation and statistical analysis

All experimental measurements, including antioxidant assays (DPPH, FRAP, and ABTS), total phenolic content (TPC), total flavonoid content (TFC), α-glucosidase inhibition, α-amylase inhibition, and LC–MS/MS analyses, were performed in triplicate. Data are presented as mean ± standard deviation (SD). Statistical differences among sample groups were evaluated using one-way analysis of variance (ANOVA). When significant differences were detected, means were compared and distinguished using different lowercase letters at a significance threshold of $p < 0.05$. Associations between biological activities and the relative abundance of annotated metabolites were examined using Pearson correlation analysis. The significance of correlation coefficients was assessed by two-tailed tests. To control for type I error due to multiple comparisons, p-values were adjusted using the Benjamini–Hochberg false discovery rate (FDR) correction procedure. All statistical analyses were performed using R software (version 4.4.0).

Molecular docking

The crystal structure of human pancreatic α-amylase (PDB ID: 4GQR; resolution: 1.20 Å) and α-glucosidase (PDB ID: 3A4A; resolution: 1.6 Å) were obtained from the RCSB PDB database

(https://www.rcsb.org/). Heteroatoms and water molecules were removed by AutoDock Tools, and polar hydrogens and Kollman charges were added to the protein macromolecule[52-54]. Ligands, identified by UPLC-MS/MS in hydroethanolic extracts of *Oenocarpus bataua* Mart., were retrieved from Pubchem and optimized with the MMFF94 force field in Avogadro v1.2.0 (https://avogadro.cc/). Input files were converted to PDB format using OpenBabel v2.4.1[55]. Molecular docking was performed with AutoDock Vina v1.2[56], defining a 42 × 42 × 42 Å grid box for protein 4GQR and a 30 × 30 × 30 Å grid box for protein 3A4A, centered on the active site (coordinates based on catalytic residues: Asp197, Glu233, Asp300 for α-amylase and Asp242, Arg315, and His280 for α-glucosidase). The protein was held rigid, whereas the ligands had rotatable bonds. For each compound, 50 independent runs were executed, with the average binding free energy (ΔG) of the 20 best poses being reported. All docking scores and binding energy values for the evaluated compounds are reported in **Supplementary Table 1**.

Ligand-receptor interactions were visualized and analyzed in 2D and 3D using Discovery Studio v24.1.0.23298 (BIOVIA, San Diego, CA, USA).

Characterization and ADMET prediction of identified compounds

The ligands from plant extract that exhibited the lowest binding energy were selected for molecular characterization and ADMET prediction. Simplified molecular line entry system (SMILES) formats for each compound were obtained from PubChem (https://pubchem.ncbi.nlm.nih.gov/) and analyzed using integrated computational tools. For pharmacokinetic (ADME, absorption, distribution, metabolism, excretion) profiling, SwissADME (http://www.swissadme.ch/)[37] and Deep-PK (https://biosig.lab.uq.edu.au/deeppk/)[57] evaluating key properties such as lipophilicity (LogP), aqueous solubility (LogS), gastrointestinal absorption (GIA), blood-brain barrier (BBB) permeability and Lipinski Rule compliance (molecular weight ≤500 Da, LogP ≤5, H donors/acceptors ≤5/10). Pharmaceutical similarity and oral drug-likeness were first assessed with SwissADME's bioavailability radar, considering polarity, size, solubility, lipophilicity, flexibility, and saturation. Subsequently, ADME and toxicity properties were predicted using the deep learning platform Deep-PK. This included metabolic interactions (CYPs 3A4, 2D6, 2C9, 1A4), transporter effects (BCRP, OATP1B1/1B3), and renal clearance[58]. Toxicity profiling covered

mutagenicity, carcinogenicity, hERG inhibition, DILI, skin/eye irritation, and ecotoxicity for *Daphnia magna*, *Tetrahymena pyriformis*, and bees[57].

Pathway analysis

Functional interpretation of the metabolomic profiles obtained from Ungurahua (*Oenocarpus bataua* Mart.) peel, seed, and pulp extracts was conducted using the Kyoto Encyclopedia of Genes and Genomes (KEGG) database (https://www.kegg.jp/), a curated resource that integrates small-molecule metabolites with metabolic pathways and associated biological functions[59].

Metabolite annotation was based on putative compound identification derived from untargeted metabolomic analysis. Pathway assignment was performed using standardized compound names consistent with KEGG nomenclature to ensure accurate mapping. Identified metabolites from each tissue were subsequently linked to KEGG metabolic pathways according to established biochemical relationships and pathway definitions.

Relative pathway representation among peel, seed, and pulp samples was evaluated by considering both the presence and relative abundance of metabolites associated with each pathway[60]. To determine statistically significant differences at the pathway level, aggregated metabolite abundances were subjected to one-way analysis of variance (ANOVA). Resulting p-values were adjusted for multiple comparisons using the Benjamini–Hochberg false discovery rate (FDR) procedure. Pathways with adjusted p-values (FDR ≤ 0.05) were considered significantly enriched or differentially represented among tissues.

A dot plot was generated to visualize pathway-level differences among tissues. In this representation, each point corresponds to a KEGG pathway; point size indicates the number of metabolites mapped to the respective pathway, while color intensity reflects the level of statistical significance after FDR correction.

All statistical analyses and graphical visualizations were performed in Python (v3.11.4) using custom scripts developed for pathway aggregation and statistical testing. The corresponding scripts

are publicly available in the GitHub repository (IKIAM-NPLab/Oenocarpus-bataua-Mart), ensuring transparency and reproducibility of the analytical workflow.

Data availability

All data generated or analyzed during this study are included in this published article and its Electronic Supplementary Information (ESI†).

Code Availability: No applicable

Acknowledgments

The authors thank the Universidad Regional Amazónica Ikiam and the Pontificia Universidad Católica del Ecuador for their support in carrying out this research.

Author contributions

Conceived the project, N.G.S.M. and K.D.-S.; visualization, N.G.S.M., K.D.-S., and P.J.E.-M.; investigation, N.G.S.M., K.D.-S., C.A.M.D., T.G., J.P.-F., R.R., K.O.-T., J.R.A., M.O.-O., P.C.-P., P.J.E.-M.; performed the experiments, C.A.M.D., T.G., J.P.-F., R.R., K.O.-T., J.R.A., M.O.-O., P.C.-P.; supervision, N.G.S.M., K.D.-S., P.C.-P., and P.J.E.-M.; data analysis and prepared figures, N.G.S.M.; conducted and analyzed the molecular docking part, K.D.-S.; writing—original draft preparation, N.G.S.M., K.D.-S.; writing—review and editing, N.G.S.M., K.D.-S., and P.J.E.-M.; project administration, N.G.S.M., K.D.-S., C.A.M.D., and P.J.E.-M., funding acquisition; N.G.S.M., K.D.-S., and P.J.E.-M. All authors critically reviewed, revised, and approved the final version of the manuscript.

Competing interest

No, I declare that the authors have no competing interests as defined by Nature Portfolio, or other interests that might be perceived to influence the results and/or discussion reported in this paper.

5. References

1 Chen, W. *et al.* Microneedle-array patches loaded with dual mineralized protein/peptide particles for type 2 diabetes therapy. *Nature Communications* **8**, 1777, doi:10.1038/s41467-017-01764-1 (2017).

2 Peytam, F. *et al.* Design, synthesis, and evaluation of novel substituted imidazo[1,2-c]quinazoline derivatives as potential α-glucosidase inhibitors with bioactivity and molecular docking insights. *Scientific Reports* **14**, 27507, doi:10.1038/s41598-024-78878-2 (2024).

3 Uti, D. E. *et al.* Natural Antidiabetic Agents: Current Evidence and Development Pathways from Medicinal Plants to Clinical use. *Natural Product Communications* **20**, 1934578X251323393, doi:10.1177/1934578x251323393 (2025).

4 Cheng, J. *et al.* Effects and mechanisms of anti-diabetic dietary natural products: an updated review. *Food & Function* **15**, 1758-1778, doi:10.1039/D3FO04505F (2024).

5 Shahzad, A. *et al.* Integrated in vitro, in silico, and in vivo approaches to elucidate the antidiabetic mechanisms of Cicer arietinum and Hordeum vulgare extract and secondary metabolites. *Scientific Reports* **15**, 6620, doi:10.1038/s41598-025-89642-5 (2025).

6 Yu, X. *et al.* Metabolite signatures of diverse Camellia sinensis tea populations. *Nature Communications*

11, 5586, doi:10.1038/s41467-020-19441-1 (2020).
7 Lima, A. d. S. *et al.* Amazonian pataua (Oenocarpus bataua) pulp extract: bioaccessibility of phenolic compounds and effects on cellular antioxidant and antimalarial activities. *Future Foods* **11**, 100650, doi:10.1016/j.fufo.2025.100650 (2025).
8 Rezaire, A. *et al.* Amazonian palm Oenocarpus bataua ("patawa"): Chemical and biological antioxidant activity – Phytochemical composition. *Food Chemistry* **149**, 62-70, doi:10.1016/j.foodchem.2013.10.077 (2014).
9 Méndez-Durazno, C. *et al.* Antioxidant Capacity through Electrochemical Methods and Chemical Composition of Oenocarpus bataua and Gustavia macarenensis from the Ecuadorian Amazon. *Antioxidants* **12**, 318, doi:10.3390/antiox12020318 (2023).
10 Ávila-Román, J. *et al.* Phenolic compounds and biological rhythms: Who takes the lead? *Trends in Food Science & Technology* **113**, 77-85, doi:10.1016/j.tifs.2021.04.050 (2021).
11 Wongnarat C & P., S. Phytochemical and Antioxidant Activity in Seeds and Pulp of Grape Cultivated in Thailand. *Orient J Chem* **33**, 113-121, doi:10.13005/ojc/330112 (2017).
12 McDougall, G. J. *et al.* Different Polyphenolic Components of Soft Fruits Inhibit α-Amylase and α-Glucosidase. *Journal of Agricultural and Food Chemistry* **53**, 2760-2766, doi:10.1021/jf0489926 (2005).
13 Clifford, M. N., Johnston, K. L., Knight, S. & Kuhnert, N. Hierarchical Scheme for LC-MSn Identification of Chlorogenic Acids. *Journal of Agricultural and Food Chemistry* **51**, 2900-2911, doi:10.1021/jf026187q (2003).
14 Davey, M. W. *et al.* Plant L-ascorbic acid: chemistry, function, metabolism, bioavailability and effects of processing. *Journal of the Science of Food and Agriculture* **80**, 825-860, doi:10.1002/(SICI)1097-0010(20000515)80:7<825::AID-JSFA598>3.0.CO;2-6 (2000).
15 de Pascual-Teresa, S., Santos-Buelga, C. & Rivas-Gonzalo, J. C. Quantitative Analysis of Flavan-3-ols in Spanish Foodstuffs and Beverages. *Journal of Agricultural and Food Chemistry* **48**, 5331-5337, doi:10.1021/jf000549h (2000).
16 Santos-Buelga, C. & Scalbert, A. Proanthocyanidins and tannin-like compounds – nature, occurrence, dietary intake and effects on nutrition and health. *Journal of the Science of Food and Agriculture* **80**, 1094-1117, doi:10.1002/(SICI)1097-0010(20000515)80:7<1094::AID-JSFA569>3.0.CO;2-1 (2000).
17 Shahidi, F. & Ambigaipalan, P. Phenolics and polyphenolics in foods, beverages and spices: Antioxidant activity and health effects – A review. *Journal of Functional Foods* **18**, 820-897, doi:10.1016/j.jff.2015.06.018 (2015).
18 Wang, L. *et al.* Glycine betaine reduces chilling injury in peach fruit by enhancing phenolic and sugar metabolisms. *Food Chemistry* **272**, 530-538, doi:10.1016/j.foodchem.2018.08.085 (2019).
19 Dixon, R. A. & Paiva, N. L. Stress-Induced Phenylpropanoid Metabolism. *The Plant Cell* **7**, 1085-1097, doi:10.1105/tpc.7.7.1085 (1995).
20 Vance, J. E. & Tasseva, G. Formation and function of phosphatidylserine and phosphatidylethanolamine in mammalian cells. *Biochimica et Biophysica Acta (BBA) - Molecular and Cell Biology of Lipids* **1831**, 543-554, doi:10.1016/j.bbalip.2012.08.016 (2013).
21 Dixon, R. A., Xie, D.-Y. & Sharma, S. B. Proanthocyanidins – a final frontier in flavonoid research? *New Phytologist* **165**, 9-28, doi:10.1111/j.1469-8137.2004.01217.x (2005).
22 Resat Atilgan, M. & Bayraktar, O. in *Handbook of Food Bioactive Ingredients: Properties and Applications* (eds Seid Mahdi Jafari, Ali Rashidinejad, & Jesus Simal-Gandara) 1-43 (Springer International Publishing, 2022).
23 Lee, S., Kim, S.-G. & Park, C.-M. Salicylic acid promotes seed germination under high salinity by modulating antioxidant activity in Arabidopsis. *New Phytologist* **188**, 626-637, doi:10.1111/j.1469-8137.2010.03378.x (2010).
24 Agati, G., Azzarello, E., Pollastri, S. & Tattini, M. Flavonoids as antioxidants in plants: location and functional significance. *Plant science : an international journal of experimental plant biology* **196**, 67-76, doi:10.1016/j.plantsci.2012.07.014 (2012).
25 Badaoui, H. *et al.* The Main Chemical Constituents Responsible for the Antidiabetic Properties of the Datura Metel L Plant. Decryption and In-silico Investigations. *Physical Chemistry Research* **13**, 241-254, doi:10.22036/pcr.2025.474045.2569 (2025).
26 Kalay, E. *et al.* Design, synthesis, and inhibition of α-glucosidase by novel L-phenylalanine-derived hydrazones: Kinetic, molecular docking, and dynamics studies. *Archives of Biochemistry and Biophysics*

768, doi:10.1016/j.abb.2025.110368 (2025).
27 Sireesha, S. M. & Beda, B. D. Design, synthesis, and antidiabetic evaluation of N-2-aryl-1,2,3-triazoles (NATs) as potent α-amylase and α-glucosidase inhibitors: a computational and biochemical investigation. *Journal of Molecular Structure* **1343**, doi:10.1016/j.molstruc.2025.142771 (2025).
28 Xu, Y., Liang, X. & Hyun, C. G. Discovery of α-glucosidase inhibitors from Paenibacillus sp. JNUCC 31 via genome mining, fatty acid profiling, and in silico analysis. *Scientific Reports* **15**, doi:10.1038/s41598-025-21753-5 (2025).
29 de los Monteros-Silva, N. E. *et al.* Unlocking the Ilex guayusa Potential: Volatile Composition, Antioxidant, Antidiabetic, and Hemolytic Activities, with In Silico Molecular Docking and ADMET Analysis of Hydroethanolic Extracts. *Molecules* **30**, 3885, doi:10.3390/molecules30193885 (2025).
30 Qaed, E. *et al.* Procyanidins: A promising anti-diabetic agent with potential benefits on glucose metabolism and diabetes complications. *Wound Rep Reg.* **31**, 688-699, doi:10.1111/wrr.13115 (2023).
31 Gonzalez-Abuin, N. *et al.* Procyanidins and their healthy protective effects against type 2 diabetes. *Current medicinal chemistry* **22**, 39-50, doi:10.2174/0929867321666140916115519 (2015).
32 Fatema, K. *et al.* In-vitro antioxidant and antidiabetic effects of Rorippa indica (L.) extract and fractions with molecular docking, dynamics simulation, ADMET, and PASS studies. *Journal of Molecular Structure* **1316**, 138868, doi:10.1016/j.molstruc.2024.138868 (2024).
33 Şahin, İ., Çeşme, M., Özgeriş, F. B. & Tümer, F. Triazole based novel molecules as potential therapeutic agents: Synthesis, characterization, biological evaluation, in-silico ADME profiling and molecular docking studies. *Chemico-Biological Interactions* **370**, doi:10.1016/j.cbi.2022.110312 (2023).
34 El-Sofany, W. I. *et al.* Novel triazole-tethered thiazol-4(5H)-one hybrids as potential therapeutics for obesity and type 2 diabetes: in vitro, in vivo, and in silico evaluations. *Journal of Molecular Structure* **1341**, doi:10.1016/j.molstruc.2025.142577 (2025).
35 Tadera, K., Minami, Y., Takamatsu, K. & Matsuoka, T. Inhibition of alpha-glucosidase and alpha-amylase by flavonoids. *Journal of nutritional science and vitaminology* **52**, 149-153, doi:10.3177/jnsv.52.149 (2006).
36 Yang, H. *et al.* Bioactive procyanidins from dietary sources: The relationship between bioactivity and polymerization degree. *Trends in Food Science & Technology* **111**, 114-127, doi:10.1016/j.tifs.2021.02.063 (2021).
37 Daina, A., Michielin, O. & Zoete, V. SwissADME: A free web tool to evaluate pharmacokinetics, drug-likeness and medicinal chemistry friendliness of small molecules. *Scientific Reports* **7**, doi:10.1038/srep42717 (2017).
38 Lipinski, C. A., Lombardo, F., Dominy, B. W. & Feeney, P. J. Experimental and computational approaches to estimate solubility and permeability in drug discovery and development settings. *Advanced Drug Delivery Reviews* **64**, 4-17, doi:10.1016/j.addr.2012.09.019 (2012).
39 Zhu, C. *et al.* Metabolic variations of organic acids, amino acids, fatty acids and aroma compounds in the pulp of different pummelo varieties. *LWT* **130**, 109445, doi:10.1016/j.lwt.2020.109445 (2020).
40 Xi, Y. *et al.* Postharvest fruit quality and antioxidants of nectarine fruit as influenced by chlorogenic acid. *LWT* **75**, 537-544, doi:10.1016/j.lwt.2016.10.004 (2017).
41 Guo, H., Li, S., Liu, Y. & Yang, Q. Catechin promotes the germination of Pistacia chinensis seeds via GA biosynthesis. *Annals of Botany* **134**, 233-246, doi:10.1093/aob/mcae061 %J Annals of Botany (2024).
42 Kupina, S., Fields, C., Roman, M. C. & Brunelle, S. L. Determination of Total Phenolic Content Using the Folin-C Assay: Single-Laboratory Validation, First Action 2017.13. *Journal of AOAC INTERNATIONAL* **101**, 1466-1472, doi:10.5740/jaoacint.18-0031 (2019).
43 Tuah, B., Asante, M., Asare, G., Doku, D. & Health. In vitro antioxidant activity in seven selected local Ghanaian spices and an artificial spice, shrimp cube. *World Journal of Nutrition* **5**, 46-52, doi:10.12691/jnh-5-2-4 (2017).
44 Brand-Williams, W., Cuvelier, M. E. & Berset, C. Use of a free radical method to evaluate antioxidant activity. *LWT - Food Science and Technology* **28**, 25-30, doi:10.1016/S0023-6438(95)80008-5 (1995).
45 Xiao, F., Xu, T., Lu, B. & Liu, R. Guidelines for antioxidant assays for food components. *Food Frontiers* **1**, 60-69, doi:10.1002/fft2.10 (2020).
46 Re, R. *et al.* Antioxidant activity applying an improved ABTS radical cation decolorization assay. *Free Radical Biology and Medicine* **26**, 1231-1237, doi:10.1016/S0891-5849(98)00315-3 (1999).
47 Benzie, I. F. F. & Strain, J. J. The Ferric Reducing Ability of Plasma (FRAP) as a Measure of "Antioxidant

Power": The FRAP Assay. *Analytical Biochemistry* **239**, 70-76, doi:https://doi.org/10.1006/abio.1996.0292 (1996).
48 Wickramaratne, M. N., Punchihewa, J. C. & Wickramaratne, D. B. M. In-vitro alpha amylase inhibitory activity of the leaf extracts of Adenanthera pavonina. *BMC Complementary and Alternative Medicine* **16**, 466, doi:10.1186/s12906-016-1452-y (2016).
49 Pistia-Brueggeman, G. & Hollingsworth, R. I. A preparation and screening strategy for glycosidase inhibitors. *Tetrahedron* **57**, 8773-8778, doi:10.1016/S0040-4020(01)00877-8 (2001).
50 Fernández, M. A. *et al.* Exploring Variability in the Methylxanthine Content within Ilex guayusa Loes: Impact of Soil Conditions, Age, and Sunlight Exposure. *ACS Agricultural Science & Technology* **5**, 1034-1046, doi:10.1021/acsagscitech.4c00778 (2025).
51 Sun, W. & Shahrajabian, M. H. Therapeutic Potential of Phenolic Compounds in Medicinal Plants—Natural Health Products for Human Health. *Molecules* **28**, 1845, doi:10.3390/molecules28041845 (2023).
52 Morris, G. M. *et al.* AutoDock4 and AutoDockTools4: Automated docking with selective receptor flexibility. *Journal of computational chemistry* **30**, 2785-2791, doi:10.1002/jcc.21256 (2009).
53 Ochoa-Ocampo, M. *et al.* Volatile Compositional Profile, Antioxidant Properties, and Molecular Docking of Ethanolic Extracts from Philodendron heleniae. *Molecules* **30**, doi:10.3390/molecules30061366 (2025).
54 Sanner, M. F. Python: a programming language for software integration and development. *Journal of molecular graphics & modelling* **17**, 57-61 (1999).
55 O'Boyle, N. M. *et al.* Open Babel: An open chemical toolbox. *Journal of Cheminformatics* **3**, 33, doi:10.1186/1758-2946-3-33 (2011).
56 Eberhardt, J., Santos-Martins, D., Tillack, A. F. & Forli, S. AutoDock Vina 1.2.0: New Docking Methods, Expanded Force Field, and Python Bindings. *Journal of Chemical Information and Modeling* **61**, 3891-3898, doi:10.1021/acs.jcim.1c00203 (2021).
57 Myung, Y., de Sá, A. G. C. & Ascher, D. B. Deep-PK: deep learning for small molecule pharmacokinetic and toxicity prediction. *Nucleic Acids Research* **52**, W469-W475, doi:10.1093/nar/gkae254 (2024).
58 González, E. *et al.* From metabolomics to molecular docking: Unveiling the antioxidant potential of Ecuadorian Hyeronima macrocarpa. *Food Chemistry: X* **33**, 103448, doi:10.1016/j.fochx.2025.103448 (2026).
59 Kanehisa, M. & Goto, S. KEGG: kyoto encyclopedia of genes and genomes. *Nucleic Acids Res* **28**, 27-30, doi:10.1093/nar/28.1.27 (2000).
60 Pastuña-Fasso, J. V. *et al.* Influence of plant age and sunlight exposure on the volatile profile and metabolomic pathways of Ilex guayusa leaves used in the traditional Amazonian beverage. *Food Chemistry* **507**, 148238, doi:10.1016/j.foodchem.2026.148238 (2026).

Supplementary Files

This is a list of supplementary files associated with this preprint. Click to download.

- supplementaryInformation.docx
- rawprimarydata.xlsx